AFIT/GAE/ENY/92D-06

The Non-Linear Dynamics of Composite Cylindrical Shells

THESIS

James M. Greer, Jr.

AFIT/GAE/ENY/92D-06

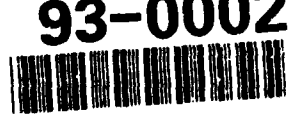

Approved for public release; distribution unlimited.

AFIT/GAE/ENY/92D-06

The Non-Linear Dynamics of Composite Cylindrical Shells

THESIS

Presented to the Faculty of the School of Engineering

of the Air Force Institute of Technology

Air University

In Partial Fulfillment of the

Requirements for the Degree of

Master of Science in Aeronautical Engineering

James M. Greer, Jr., B.S.

December, 1992

Acknowledgments

This thesis is part of a research project on the dynamic behavior of suddenly loaded composite shells; Dr. Anthony Palazotto, AFIT/ENY, principal investigator.

I wish to thank Dr. Palazotto for his expertise, guidance, and genuine concern throughout research; my thesis committee members Dr. Oxley and Dr. Torvik; Capt Scott Schimmels for enduring my frequent interruptions and patiently explaining the ins and outs of the SHELL program despite his workload in pursuing his doctoral studies; Messrs. Vin Loi and Ron Gordon for keeping the SUN workstations up and running, and for graciously solving those problems of "operator error." I would also like to thank Major Scott Dennis (Ph.D.) who authored the SHELL finite element code used in this work; Dr. C.T. Tsai, who created DSHELL from SHELL, giving the program a dynamic analysis capability; the many other AFIT faculty and staff who endured my barrages of questions; and my wonderful classmates.

Many thanks to Mr. Nelson Wolfe of the Flight Dynamics Laboratory for his generous offerings of CRAY computer time, without which this work would not have been possible.

I thank God for His mercy to me and for my wife and family. I'm particularly grateful and most indebted to my wife, Denise, for her uncomplaining support and encouragement throughout this often time consuming process. Her prayers and kind words sustained me through many long days and nights, and she had the unique ability to empathize with my struggles, having gone through the AFIT process*or* herself. Finally, thanks to my two young boys, Drew and Josh, whose smiles gave every day (no matter how rough) a happy ending.

James M. Greer, Jr.

Table of Contents

List of Figures

List of Tables

List of Symbols

Symbol	Page
τ_1	2-22
τ_{max}	2-22
τ	2-22
r	3-3
$\vec{\mathbf{f}}$	3-11
f_h	3-14
τ_h	3-14
f_1	4-5
e_{tol}	4-5
I_{tot}	4-21
$\bar{I}$	4-21
Δt_{post}	4-21
$\vec{\mathbf{V}}_i$	A-2
Δ_i	A-2
$\hat{\mathbf{e}}_i$	A-2

Abstract

The non-linear dynamic behavior of suddenly loaded composite shells is the subject of this research. The objective of the research is two-fold: (1) to characterize the apparently random physical behavior sometimes observed in the finite element analysis as either numerical instability, chaotic behavior, or both; and (2) to develop criteria for choosing time steps for the finite element model, referred to as DSHELL. This displacement based finite element code is capable of dynamic analysis of plates, arches, and cylindrical shells undergoing large displacements and moderately large rotations during deformation. DSHELL uses a 36-DOF isoparametric shell element to obtain numerical results. A simplified shell model (MSHELL) is developed to provide a shell analog that requires much less computer time to run than the full-up finite element model. The results of the investigations using this simplified model are then applied toward understanding behavior seen in the finite element code. The simplified model and the composite shell exhibit chaotic behavior after collapse. For loads not sufficient to cause collapse, the composite shell experiences oscillations at the panel edges of a type associated with near-chaotic behavior. Significant in-plane oscillations (parametric resonances) are exhibited by the suddenly-loaded composite shell. Extensive use of the *Fast Fourier Transform* (FFT) is made to investigate behavior of the MSHELL and DSHELL models in the frequency domain. The composite shell is compared to an isotropic shell of identical physical dimensions and static collapse strength, showing the primary effect of isotropy to be increased flexibility in all displacement directions. A method is developed using MSHELL for choosing appropriate time steps for analyses using DSHELL.

The Non-Linear Dynamics of Composite Cylindrical Shells

I. INTRODUCTION

The use of laminated composite materials in structures continues to grow. The high strength-to-weight ratios offered by these materials makes them ideally suited to aerospace applications. One of the ways laminated fiber composites achieve this property is to orient the fibers in preferred directions depending upon the required strength of the material and its load-bearing orientation. This technique, however, often renders the optimized composite substantially weaker in the non-preferred directions than its metallic counterpart, making dynamic stability an issue (9:1).

Most research involving the study of shell structures from a dynamic point of view exploits the shell's definition—it is thin. That is, the thickness dimension is much smaller than the shell's other dimensions. In many cases, this assumption allows the analyst to treat some quantities as negligible compared to others. In these approaches, the in-plane activity of the shell (displacements, strains, and stresses) are assumed to be much more important than through-the-thickness phenomena. The outgrowth of this approach is a method of describing the behavior of the shell by reference to the behavior of its midsurface (or datum surface). In many cases, particularly those dealing with small displacements and/or isotropic materials, this method is sufficient. However, the analysis of laminated composite materials, where material properties may vary drastically through the shell's thickness dimension, requires careful evaluation of which quantities may or may not be neglected.

1.1 Nonlinear Dynamics

If the analyst is interested in postbuckling behavior, simple linear bifurcation buckling analyses will not suffice, and solution of the nonlinear equations resulting from a collapse analysis will be required (9:2). Axially loaded columns and edge loaded flat plates both exhibit instabilities characterized by very small deformation prior to buckling. On the other hand, transversely loaded shell

structures may change shape and stress distribution significantly prior to collapse. Attempting to find the critical collapse load of shells through linear bifurcation techniques are often significantly in error (19:234).

Through linear eigenvalue analysis using equilibrium or energy methods the critical collapse load, P_c , of many simple structures may be solved for in closed form. However, the calculated value of P_c may be very much at odds with experimental values which are often only 1/3 as much as the calculated value. Furthermore, the experimental data frequently have large amounts of scatter. For some 30 years, the discrepancy between experimental and calculated values of P_c baffled investigators. The source of the discrepancy was found to be the nature of the initial postbuckling branching. If the postbuckling branching was stable (i.e., increasing the displacement required increasing the load) then the calculated and experimental data agreed fairly well. If the postbuckling branching was unstable (i.e., increasing the displacement required decreasing the load) then the calculated and experimental data were frequently at odds. (10:409–413)

Figure 3.1 on page 3-2 illustrates the type of behavior seen in unstable buckling. In those portions of the curve where the slope dP/dw is negative, a decrease in load, P , is required to reach an equilibrium state at increased deflection. It is for this reason that buckling shells and shell-like structures (like the simplified model used in the present research) are not correctly analyzed using linear bifurcation techniques.

1.2 Chaos

Another interesting feature of the dynamic analysis of shells has been the appearance of chaoslike phenomena. ***Chaos*** is the term used to define the behavior of dynamical systems whose motion cannot be predicted far into the future (17:1). There is a difference, however, between so-called random and chaotic motions. The former term is reserved for cases where parameters may be ill-defined or unknown except in perhaps a statistical sense. The term *chaotic* is reserved

for those cases where the there are no unpredictable inputs or system parameters (17:3). Chaotic motion includes the following characteristics (17:262):

1. The motion is sensitive to changes in initial conditions
2. Trajectories starting from slightly different initial conditions diverge exponentially
3. The Lyapunov exponent for the motion is positive

Many physical systems exhibit chaotic vibrations, including the vibrations of buckled elastic structures (17:9).

The nonlinear equations of equilibrium derived for the DSHELL finite element model have both of the necessary ingredients for chaos: (a) at least three independent dynamical variables (DSHELL has seven) and (b) nonlinear terms in the coupled equations (there are many). Meeting these criteria admits the following behavior (2:3):

- trajectories in phase space may diverge
- confinement (boundedness) of motion to a finite region of the phase space
- uniqueness of the trajectory, with the added feature that two trajectories corresponding to similar energies will pass very close to each other, *but the orbits will not cross each other.*

Taylor (28) and others have witnessed an apparently random behavior in both pre- and post-buckled states, and the present research shows that there are two sources of this behavior — one of them being chaoslike. The deformed geometries of the shell structures differ markedly depending upon whether the random behavior is due to chaos or numerical instability.

1.3 Analytical Method

An analysis of the laminated composite shell subjected to a sudden transverse load could take many forms depending on how the problem is cast. Table 1.1 outlines some of the problem features and the associated considerations.

Feature	Consideration
magnitude of displacements and rotations	geometric linearity
magnitude of strains; material properties	material linearity; plasticity
rates of strain; time dependency	creep and stress relaxation (viscoelasticity)
temperature; temperature changes	thermal effects

Table 1.1. Features and considerations for analysis

Of the considerations in Table 1.1, only geometric nonlinearity is addressed in the present research. Displacements and rotations are large, so even if small strains allow the assumption of material linearity, geometric linearity cannot be claimed.

The variation of the total potential energy is used to develop the governing equations for the laminated composite shell. The result of applying this technique is five coupled nonlinear partial differential equations that describe the shell's equilibrium. The finite element method is a powerful numerical tool for solving such equations, and hence is the method of choice for the current research (9:78). The finite element code is computationally intensive, often modelling hundreds of nonlinearly interacting degrees of freedom (DOF). The matrix manipulations require large amounts of computational storage and time. For this reason, the MSHELL simplified model is developed as an analog to the finite element model. The MSHELL simplified model has many of the shell's features, but requires comparatively little computational time. Hence, long simulations may be performed using MSHELL in an attempt to characterize the phenomena seen in the finite element code.

1.4 *Previous Work*

The development of shell theory has its roots in plate theory, the plate being a special case of the shell (a shell with infinite radius of curvature in all in-plane directions). Many theories have been developed to treat the behavior of plates and shells. Each has certain advantages and drawbacks, and each has some limited range of applicability. The most general equations of elasticity governing the behavior of plates and shells are cumbersome, and for this reason each theory trades at some point on applicability (generality) versus ease of use.

Recent work in the area of shell dynamics is wide-ranging. Simitses (26) offers an elegant analytical treatment of thin laminated shells (wherein each lamina is orthotropic) subjected to sudden loads. Based upon his general assumptions, he derives the field equations based upon Donnell-type kinematic relations. He assumes normals to the shell surface remain normal after deformation, thus neglecting through the thickness shear, and further restricts the problem to small strains and small rotations. He presents a closed form static solution methodology as well as a finite difference dynamic solution methodology for the thin shell. Simitses also describes the phenomenon of ***parametric resonance***, in which the forcing function causes "...a resonance in a secondary mode of vibration or a mode other than the one directly excited by its presence." (26:260). This is seen in the transversely loaded cylindrical shell, which not only oscillates in the transverse direction, but experiences in-plane oscillations as well.

A perturbation procedure is used by Raouf and Palazotto (21) to derive a set of asymptotically consistent nonlinear equations of motion describing the nonlinear dynamics of an arbitrarily laminated composite cylindrical shell in cylindrical bending. Unlike the present research, in which transverse shear strains are allowed while strain in the thickness direction is not, Raouf and Palazotto prohibit transverse shear strains but allow for slight compressibility of the panel. The three-dimensional shell equations of elasticity are reduced to two-dimensional field equations for the panel using an order of magnitude study. The analysis reveals a threshold value for the ampli-

tude of excitation that causes saturation of the amplitude of the directly excited mode, resulting in a nonlinear response of the coupled mode which eventually dominates the response. In subsequent work, Raouf and Palazotto (20) take the quadratic nonlinearities used in the perturbation procedure and perform a single-mode spatial discretization to derive a nonlinear equation with quadratic *and* cubic nonlinearities. The results of this study of a symmetrically laminated eight-ply graphite/epoxy cylindrical shell panel show that nonlinearities of the hardening type are present even for small-amplitude oscillations. It had been thought that linear analysis was sufficient for such cases.

Palazotto and Dennis (19) and Reddy and Liu (22) have both presented higher order theories incorporating transverse shear effects, and this is certainly a key feature of the DSHELL model used in the current research. Incorporating transverse shear effects removes the limits on the magnitudes of deformations required by first-order theory. Tsai and Palazotto (30) compared the results of this 36 degree-of-freedom thin shell element based code with analyses from other sources, demonstrating the validity and accuracy of the model.

Smith (27) investigated eight variations of higher-order theory for cylindrical shells. He showed that while higher-order effects are significant during the collapse phase of the static load-displacement equilibrium, the extra computational burden imposed is excessive for typical engineering problems. The SHELL code uses only the linear terms of the transverse shear strain equations, but uses cubic displacement equations (see Section 2.1.1).

Silva used SHELL to investigate (statically) the behavior of cross- and angle-ply laminates with different boundary conditions, evaluating some 48 different cases. He demonstrates that transverse shear has a significant effect on the deformation of composite shells subjected to a transverse load, and that the angle-ply laminate developed more transverse shear strain than the cross-ply. Silva also used the Donnell shell equations to show how they develop significant inaccuracy when the rotations of the midsurface exceed about 15°. He also shows that the angle-ply laminate can-

not be successfully modeled using symmetry because the twisting generated by the 45° plies is not captured (25).

Palazotto, et al. (18) used DSHELL to study dynamic behavior of composite arches and shells, demonstrating the importance of dynamic analysis (rather than static) in exploring the shell buckling phenomenon. Shell depth and effects of anisotropy were examined in analyzing the shell snapping phenomenon, during which energy is transferred from the potential to the kinetic as the applied load reaches a critical value.

Chien and Palazotto (6) investigated dynamic buckling of composite cylindrical shells subjected to a step loading. They found that the dynamic buckling load of the model could be found through an evaluation of the motion at the node under the transverse load. For a multi-degree-of-freedom system, the existence of at least one eigenvalue with a positive real part in the Jacobian matrix associated with the Hamiltonian equation indicates dynamic instability, but Chien and Palazotto found that motion at a single degree of freedom could be evaluated for several step loads to develop a "dynamic equilibrium curve" that could predict the dynamic snap (or collapse) load (6:723). This procedure is used cautiously, and other arbitrary degrees of freedom are checked for the potential occurrence of parametric resonance. The equation defining dynamic instability is shown to be

$$\dot{w}_p = \ddot{w}_p = 0 \tag{1.1}$$

where $\dot{w}_p$ and $\ddot{w}_p$ represent the velocity and acceleration at the degree of freedom in question. They show that the presence of an inflection point in the displacement versus time curve is equivalent to this dynamic buckling criterion. Cross-ply laminates are investigated in the form of an arch and a cylindrical shell, as is the isotropic panel.

Maestrello, et al. (16), found panels of aluminum and composite material vibrated chaotically when subjected to acoustic excitation. By varying the sound pressure level, they were able to observe the transition from linear to nonlinear to chaotic vibrations. In the transition from linear

to nonlinear vibration they note the appearance of many sub-harmonics in the frequency response of the panel. A method formulated by Zeng, et al. (32) was used to estimate the Lyapunov exponents from their limited data, and the results indicated very chaotic behavior under certain conditions.

Blair, et al. (4) used a two rigid-link model to explore the nonlinear dynamic response of shallow arches, finding regions of chaotic motion. They used the method of harmonic balance, coupled with a continuation scheme to find solutions to a wide range of externally applied forcing functions.

Currently at AFIT, Captain Scott Schimmels is developing codes to incorporate plasticity in the finite element analysis of plates, arches, shells, and spherical caps. This capability represents a valuable addition to the understanding of composite behavior with material nonlinearity.

1.5 Current Work

The subject of the current research is two-fold. Previous investigators using the DSHELL code have seen dynamic behavior that is apparently unstable. One goal of the current research is to analyze this behavior and classify its origin as numerical or dynamical. Some of the behavior is chaoslike in nature. The other thrust of the research is toward understanding numerical considerations in using the DSHELL program. Key numerical parameters include the time step, Δt, the Newton-Raphson convergence tolerance, e_{tol}, and the coefficients of the beta-m differential equation solver, β_i. In the current research, the only numerical parameter examined in detail is the time step with the goal of developing criteria for generating useful results in a minimum of computer time.

The DSHELL model takes a considerable amount of computer time to run, and studies of long-term responses to loads are not practical. Because of this, the MSHELL simplified model was developed as an analog to the composite shell model. The MSHELL model allows for long-term study and, by substituting a sinusoidal load for a step load, can mimic the behavior of a node in

the shell's finite element model. The computers used in the study were the SUN SPARCstation 330 and the CRAY X-MP/216.

II. THEORY

2.1 Nonlinear Shell Analysis

"Finite elements for shells have been among the most difficult to devise." (8:341) There have been three families of approaches to the development of these elements.

1. Flat elements: Plane bending elements with plane membrane element
2. Curved elements: Classical shell theory
3. Mindlin-type elements: Special (degenerated) forms of solid elements

The DSHELL program, used in the current research, uses an element which falls into the third category. The interested reader is referred to Dennis (9:78) for a complete development of the theory behind this finite element code. A description of the displacement equations, the 36 degree of freedom (DOF) isoparametric element, and the numerical solving and integration schemes are included here for clarity.

The shell geometry is shown in Figure 2.1. The shell thickness is h , the in-plane coordinates are x and s , and the depth coordinate z (not shown) is positive toward the center of curvature. The angle Φ represents the fiber orientation angle, so that $\Phi = 0$ represents a ply whose fibers are aligned with the x (longitudinal) axis. In the text, subscripts '1' and 'x' are used interchangeably, as are the subscripts '2' and 's'.

2.1.1 DSHELL Displacement Equations. Contracted notation as described by Table 2.1 is used in the following discussion, where the σ_{ij} represent stresses and the ϵ_{ij} represent strains. The DSHELL displacement equations are derived from the general curvilinear strain-displacement relations described in Saada (24:136–137) with the following assumptions.

1. The shell is in a modified[1] state of plane stress where $\sigma_3 = 0$ (hence $\epsilon_3 = 0$).

[1] 'Modified' in the sense that in this case, through the thickness shear stresses are not neglected.

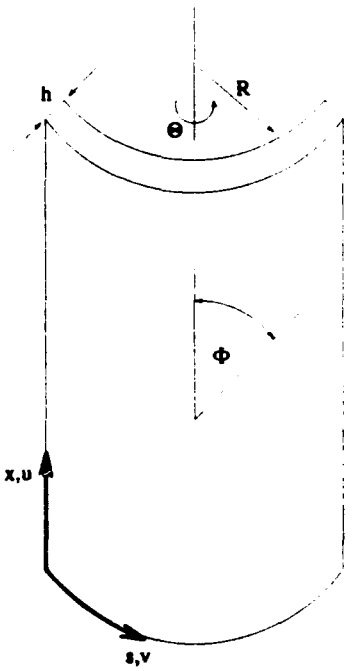

Figure 2.1. Shell geometry

STRESS		STRAIN		CYLINDRICAL
EXPLICIT	CONTRACTED	EXPLICIT	CONTRACTED	COORDINATES
σ_{11}	σ_1	ϵ_{11}	ϵ_1	x→1
σ_{22}	σ_2	ϵ_{22}	ϵ_2	s→2
σ_{33}	σ_3	ϵ_{33}	ϵ_3	z→3
σ_{23}	σ_4	$2\epsilon_{23} = \gamma_{23}$	ϵ_4	s-z→4
σ_{13}	σ_5	$2\epsilon_{13} = \gamma_{13}$	ϵ_5	x-z→5
σ_{12}	σ_6	$2\epsilon_{12} = \gamma_{12}$	ϵ_6	x-s→6

Table 2.1. Contracted notation for stresses and strains

2. The transverse shear stresses, σ_4 and σ_5, are allowed to be small nonzero values which vary parabolically through the shell thickness, vanishing at the shell surfaces.

3. Only linear terms are retained in the strain-displacement equations for ϵ_4 and ϵ_5.

4. Because $\epsilon_3 = 0$, the transverse displacement, w, is assumed constant through the shell thickness.

5. The ratio of the shell thickness, h, to the shell radius of curvature, R , is $h/R \leq 1/5$.

With these assumptions, the displacement equations may be written as (19:39)

$$\begin{aligned} u(x,\theta,z) &= u_0 + z\Psi_1 - \frac{4}{3h^2}z^3(\Psi_1 + w_{,1}) \\ v(x,\theta,z) &= v_0\left[1 - \frac{z}{R}\right] + \frac{4}{3h^2}z^3(\Psi_2 + w_{,2}) \\ w(x,\theta) &= w \end{aligned} \tag{2.1}$$

where

- u_0 is the displacement in the x coordinate direction at the shell midsurface
- v_0 is the displacement in the s, or circumferential, coordinate direction at the midsurface
- z is the distance from the shell midsurface
- u is the displacement in the x coordinate direction
- v is the displacement in the s coordinate direction
- w is the transverse displacement in the z direction
- $w_{,1}$ is the slope $\partial w/\partial x$ at the node
- $w_{,2}$ is the slope $\partial w/\partial s$ at the node
- Ψ_1 is the rotation of the normal to the shell surface in the x direction (about the s axis)
- Ψ_2 is the rotation of the normal to the shell surface in the s direction (about the x axis)

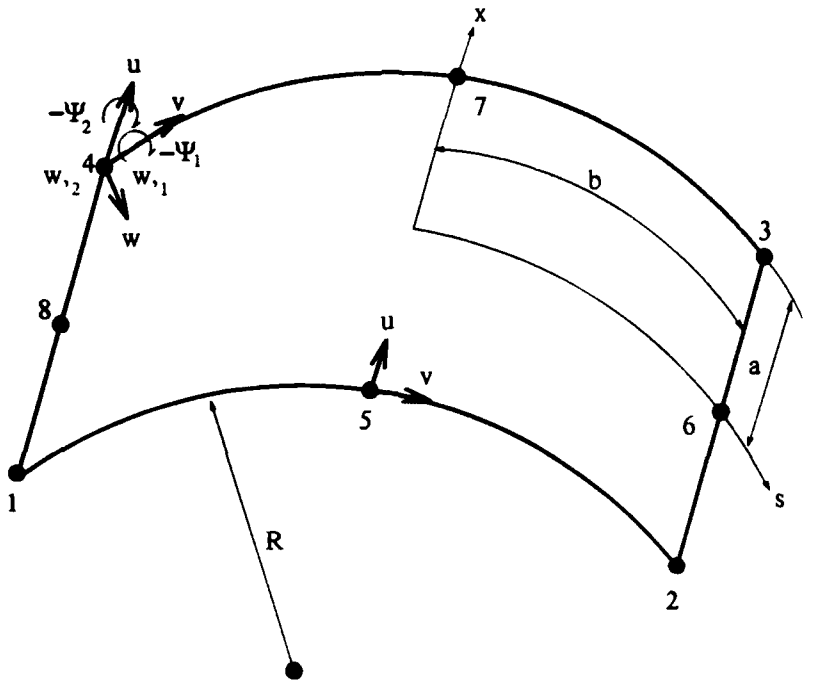

Figure 2.2. The 36-DOF isoparametric shell element

2.1.2 The 36-DOF Isoparametric Element. The finite element used in the DSHELL code is derived through energy methods. The finite element method allows the five coupled nonlinear partial differential equations representing the shell's equilibrium to be reduced to coupled nonlinear algebraic equations (19:69). The finite element used in the DSHELL code is depicted in Figure 2.2. The isoparametric element has seven DOF at each corner, while the mid-side nodes have only the u and v DOF.

*2.1.3 The Beta-*m *Method.* A numerical technique, the beta-m method (13) is employed to solve the second-order differential matrix equation

$$\mathbf{M}\ddot{\mathbf{x}} + \mathbf{C}\dot{\mathbf{x}} + \mathbf{K}\mathbf{x} = \mathbf{F}(\mathbf{t}) \tag{2.2}$$

where $\mathbf{x}$, $\dot{\mathbf{x}}$, and $\ddot{\mathbf{x}}$ represent the nodal displacement, velocity, and acceleration vectors. The mass matrix, $\mathbf{M}$, is of the *consistent* type, wherein the same shape functions used to generate the element stiffness matrices are used to generate the mass matrix (8:370). The lumped mass matrix approach is not suitable for the current research, as rotary inertia would have to be arbitrarily assigned to the nodes to capture the forces generated by rotational degrees of freedom. The damping matrix, $\mathbf{C}$, is generated using a proportional damping scheme in which

$$\mathbf{C} = 2\xi\omega\mathbf{M} \tag{2.3}$$

Where ξ is the damping ratio and ω is the linear fundamental natural frequency (6:727). The displacement vector, $\mathbf{x}$, (for an r-noded mesh), is of the form (superscripts denote node numbers, not powers)

$$\mathbf{x} = \left\{ \begin{array}{cccccccccccccccc} u^1 & v^1 & w^1 & w^1{}_{,1} & w^1{}_{,2} & \Psi_1^1 & \Psi_2^1 & u^2 & v^2 & \cdots & u^r & v^r & w^r & w^r{}_{,1} & w^r{}_{,2} & \Psi_1^r & \Psi_2^r \end{array} \right\}^{\mathrm{T}} \tag{2.4}$$

The beta-m method offers several advantages: (1) it is a single step method, i.e. it needs data from only the most recent time step to calculate parameters for the next time step, (2) it is a very general method, i.e. the choice of parameters $\beta_1, \beta_2, \ldots, \beta_{m-1}$ not only govern the stability and accuracy characteristics of the method, but allow the user to select from a broad range of implicit or explicit algorithms which are sub-families to the beta-m method, and (3) the finite difference scheme is not required for this method. The beta-m method is defined by[2] (30:383-384)

$$\mathbf{x}_{n+1}^{(k)} = \mathbf{q}_k + b_k \Delta \mathbf{x}^{(m)} \tag{2.5}$$

[2]Indices in parenthesis indicate order of derivative, not exponents.

where

$$\mathbf{q}_k = \sum_{j=k}^{m} \mathbf{x}_n^{(j)} h^{j-k}/(j-k)! \tag{2.6}$$

and

$$b_k = \beta_k h^{m-k}/(m-k)! \tag{2.7}$$

and $k = 0, 1, \ldots, m$. The value of β_m is always taken to be unity, and h is the time increment for each time step. The method of order m implies that $\mathbf{x}_n^{(m)}$ is the highest derivative to be retained. The terms above relate the displacement, velocity, and acceleration at time step $n+1$ to their values at time step n and the unknown change in acceleration, $\Delta\ddot{\mathbf{x}}$, as follows:

$$\mathbf{x}_{n+1} = \mathbf{x}_n + \dot{\mathbf{x}}_n h + \frac{1}{2}\ddot{\mathbf{x}}_n h^2 + \frac{1}{2}\beta_0 h^2 \Delta\ddot{\mathbf{x}} \tag{2.8}$$

$$\dot{\mathbf{x}}_{n+1} = \dot{\mathbf{x}}_n + \ddot{\mathbf{x}}_n h + \beta_1 h \Delta\ddot{\mathbf{x}} \tag{2.9}$$

$$\ddot{\mathbf{x}}_{n+1} = \ddot{\mathbf{x}}_n + \Delta\ddot{\mathbf{x}} \tag{2.10}$$

Substituting Eq (2.5) into Eq (2.2) at time t_{n+1} yields

$$\left[b_2\mathbf{M} + b_1\mathbf{C} + b_0\mathbf{K}\left(\mathbf{q}_0 + b_0\Delta\ddot{\mathbf{x}}\right)\right]\Delta\ddot{\mathbf{x}} = \mathbf{F}_{n+1} - \left\{\mathbf{M}\mathbf{q}_2 + \mathbf{C}\mathbf{q}_1 + \mathbf{K}\left(\mathbf{q}_0 + b_0\Delta\ddot{\mathbf{x}}\right)\mathbf{q}_0\right\} \tag{2.11}$$

where $\mathbf{F}_{n+1}$ is the applied load vector at time t_{n+1}. Eq (2.11) represents a set of nonlinear algebraic equations, and the Newton-Raphson iterative method is employed to solve it (12:66). At each time step, we assume

$$\Delta\ddot{\mathbf{x}}_{i+1} = \Delta\ddot{\mathbf{x}}_i + \delta\ddot{\mathbf{x}}_i \tag{2.12}$$

where i is the iteration number within a single time step. Applying this to Eq (2.11) we have

$$\left[b_2\mathbf{M} + b_1\mathbf{C} + b_0\mathbf{K}_T\left(\mathbf{q}_0 + b_0\Delta\ddot{\mathbf{x}}_i\right)\right]\delta\ddot{\mathbf{x}}_i =$$

$$\mathbf{F}_{n+1} - \mathbf{M}\left\{\mathbf{q}_2 + b_2\Delta\ddot{\mathbf{x}}_i\right\} - \mathbf{C}\left\{\mathbf{q}_1 + b_1\Delta\ddot{\mathbf{x}}_i\right\} - \mathbf{K}\left(\mathbf{q}_0 + b_0\Delta\ddot{\mathbf{x}}\right)\left\{\mathbf{q}_0 + b_0\Delta\ddot{\mathbf{x}}_i\right\} \tag{2.13}$$

where $\mathbf{K}_T(\mathbf{x})$ is a tangential stiffness matrix evaluated using the displacements $\mathbf{x}$, which is

$$K_T(\mathbf{x}) = K_0 + K_1(\mathbf{x}) + K_2(\mathbf{x}) \tag{2.14}$$

Eq (2.13) is then solved using the following algorithm

1. Given $\mathbf{x}_n$, $\dot{\mathbf{x}}_n$, and $\ddot{\mathbf{x}}_n$ at time t_n, we seek solutions at t_{n+1}.
2. Calculate $\mathbf{q}_0$, $\mathbf{q}_1$, and $\mathbf{q}_2$ from Eq (2.6).
3. Given $\Delta\ddot{\mathbf{x}}$ and $\mathbf{x}_{n+1}$ from the ith iteration, we obtain the right-hand-side of Eq (2.13), and the updated tangential stiffness matrix from Eq (2.14).
4. Solve for the primary unknown, $\delta\ddot{\mathbf{x}}_i$ from Eq (2.13).
5. Calculate the updated solution vector $\delta\ddot{\mathbf{x}}_{i+1}$ from Eq (2.12).
6. Update $\mathbf{x}_{n+1}$, $\dot{\mathbf{x}}_{n+1}$, and $\ddot{\mathbf{x}}_{n+1}$ for the $(i+1)$th iteration from Eq (2.5).
7. If

$$\frac{\left|\left(\sqrt{\sum_{j=1}^{r}(\mathbf{x}_{n+1})_j^2}\right)_{i+1} - \left(\sqrt{\sum_{j=1}^{r}(\mathbf{x}_{n+1})_j^2}\right)_i\right|}{\left(\sqrt{\sum_{j=1}^{r}(\mathbf{x}_{n+1})_j^2}\right)_i} \leq \epsilon \tag{2.15}$$

go to step (1) for the next time step, otherwise go to step (3) for the next iteration. The value of j is the degree of freedom number and r is the total number of degrees of freedom in the model. The value of ϵ is chosen by the user and represents the maximum acceptable convergence tolerance.

2.2 A Simplified Shell Model

The DSHELL finite element model incorporates many complex nonlinear phenomena involving hundreds or even thousands of active and interacting degrees of freedom. Over ten thousand lines of code are executed to perform just one iteration in one time step, using large amounts of computer memory and time. It would be desirable to have a simpler analogy to use as a tool to

understand some of the results produced by DSHELL. To this end, another computer program was developed to try to model some of the important features of shell behavior on a smaller and more easily analyzed scale.

The model described herein, referred to as 'MSHELL', incorporates some of the important features of the laminated cylindrical shell:

- The 'snap-through' phenomena is facilitated.
- Stiffness exists in both in-plane directions, as well as in the transverse direction.
- The equations of motion for this system are nonlinear though, as in the finite element program, the material properties (in this case, the spring stiffness) are linear.
- The coupled equations meet the criteria for admitting chaotic behavior.

The model does not mimic the cylindrical shell in these important ways:

- The differences in material properties through the laminate thickness are not modeled, as no thickness related parameters exist
- The shell's resistance to transverse displacement due to its width (in the longitudinal direction) is not modeled. (The model is more 'arch-like' than 'shell-like' in this regard.)
- The distributed mass of the cylindrical shell is not modeled.
- The interactions of the motions at various points is not modeled, though interactions of nodes in the suddenly loaded shell may be effectively simulated through sinusoidal loading of the model.

2.2.1 Equations of Motion. The equations of motion are purposefully derived from kinematic considerations rather than energy because it is desired to use energy balance as a checking mechanism.

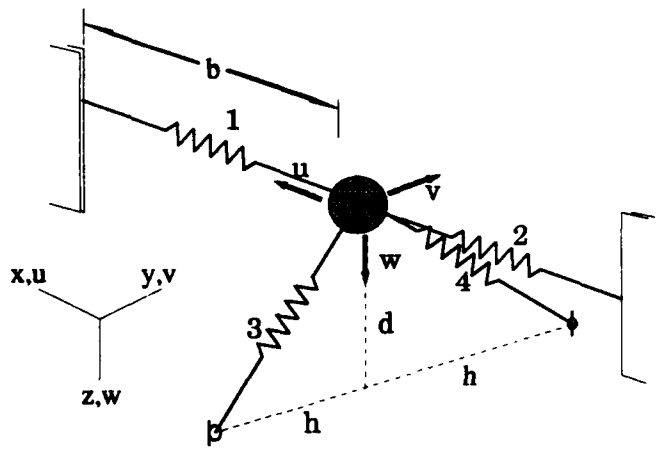

Figure 2.3. Simplified model of shell

The model is depicted in Figure 2.3, and its appearance as it relates to the shell geometry is shown in Figure 2.4. All springs are of undeformed length b, and springs 1 and 2 remain horizontal (in the $x-y$ plane) regardless of the deformed geometry, such that the ends of springs 1 and 2 can be thought of as riding in tracks of infinite length offering no resistance to vertical motion of the spring ends. The goal here was to try to keep the model as simple as possible while still capturing the nonlinear effects. Attempting to introduce additional transverse stiffness due to springs 1 and 2 severely complicated the model, though it should be noted that this feature explicitly decouples longitudinal and transverse stiffnesses. The object is of mass m , and the dimensions h and d are the projections of undeformed spring 3 (or 4) on the horizontal and vertical, respectively.

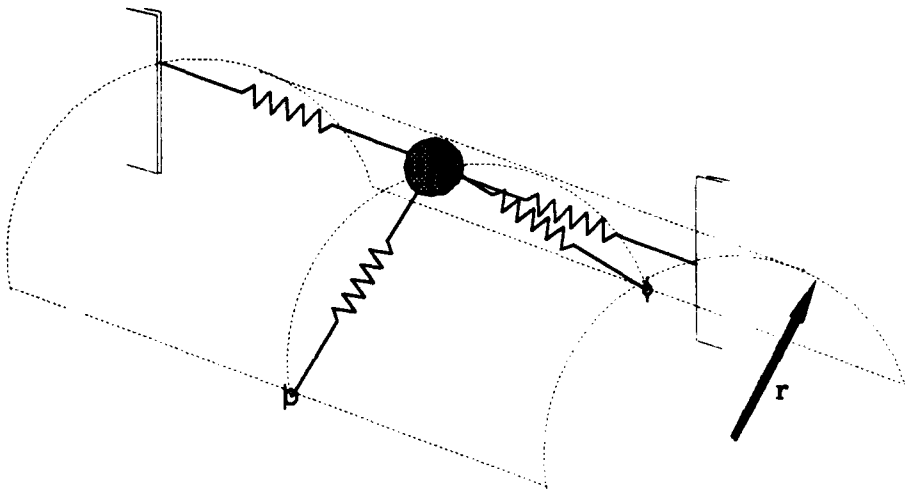

Figure 2.4. Simplified model of shell as it relates to geometry of shell, radius r

The equations of motion for the model are

$$\ddot{u}(u, v, w, \dot{u}, f_u(t)) =$$
$$(1/m)\left[f_u + bk_1 - \frac{b^2k_1}{b_1} - bk_2 + \frac{b^2k_2}{b_2} + \left(-k_1 + \frac{bk_1}{b_1} - k_2 + \frac{bk_2}{b_2} - k_3 + \frac{bk_3}{b_3} - k_4 + \frac{bk_4}{b_4}\right)u - c\dot{u}\right] \quad (2.16)$$

$$\ddot{v}(u, v, w, \dot{v}, f_v(t)) =$$
$$(1/m)\left[f_v - hk_3 + \frac{bhk_3}{b_3} + hk_4 - \frac{bhk_4}{b_4} + \left(-k_1 + \frac{bk_1}{b_1} - k_2 + \frac{bk_2}{b_2} - k_3 + \frac{bk_3}{b_3} - k_4 + \frac{bk_4}{b_4}\right)v - c\dot{v}\right] \quad (2.17)$$

$$\ddot{w}(u, v, w, \dot{w}, f_w(t)) =$$
$$(1/m)\left[f_w + dk_3 - \frac{bdk_3}{b_3} + dk_4 - \frac{bdk_4}{b_4} + \left(-k_3 + \frac{bk_3}{b_3} - k_4 + \frac{bk_4}{b_4}\right)w - c\dot{w}\right] \quad (2.18)$$

where the variables are defined as follows:

- u, v, and w are the displacements in the x, y, and z coordinate directions respectively.
- The dots represent derivatives with respect to time, e.g. $\dot{u} = \mathrm{d}u/\mathrm{d}t$.
- The k_i represent the linear spring stiffnesses.
- b is the undeformed spring length, and is the same for all springs.
- The b_i are the deformed spring lengths, the equations for which are found in Eq (A.1) on page A-1.
- h is the projection of undeformed spring 3 (or 4) on to the y coordinate direction.
- d is the projection onto the z coordinate direction.
- c is the viscous damping coefficient
- The f_i are the time varying components of the applied force.

The derivation of the equations of motion is provided as Appendix A.

2.2.2 Static Collapse Load. Calculation of the static collapse load is not difficult with this model. The total static spring force in the w direction due to springs 3 and 4 (in the presence of only a w displacement) is given by

$$f_{spring} = \frac{-2k\left[-b+\sqrt{h^2+(d-w)^2}\right](d-w)}{\sqrt{h^2+(d-w)^2}} \tag{2.19}$$

Its derivative, found using the D command in *Mathematica*[3] (3:52), is

$$\frac{d}{dw}f_{spring} = \frac{2k\left(-b+\sqrt{h^2+(d-w)^2}\right)}{\sqrt{h^2+(d-w)^2}} - \frac{2k\left(-b+\sqrt{h^2+(d-w)^2}\right)(d-w)^2}{\left(h^2+(d-w)^2\right)^{\frac{3}{2}}} +$$

[3] *Mathematica* is a registered trademark of Wolfram Research, Inc.

$$+\frac{2k(d-w)^2}{h^2+(d-w)^2}$$

The real roots of this derivative, using the *Solve* command in *Mathematica* (3:46) are

$$w_1 = \frac{2d + 2\sqrt{b^{\frac{2}{3}} - h^{\frac{2}{3}}}h^{\frac{2}{3}}}{2}, \qquad w_2 = \frac{2d - 2\sqrt{b^{\frac{2}{3}} - h^{\frac{2}{3}}}h^{\frac{2}{3}}}{2} \tag{2.20}$$

The displacement at the static snapping load is given by w_2, for exceeding this displacement moves us to the unstable portion of the equilibrium curve ($dP/dw < 0$):

$$w(f_{max}) = \frac{2d - 2\sqrt{b^{\frac{2}{3}} - h^{\frac{2}{3}}}h^{\frac{2}{3}}}{2} \tag{2.21}$$

Substituting this value into Eq (2.19) yields

$$f_{snap} = \frac{2\sqrt{b^{\frac{2}{3}} - h^{\frac{2}{3}}}h^{\frac{2}{3}}\left(b - \sqrt{b^{\frac{2}{3}}h^{\frac{4}{3}}}\right)k}{\sqrt{b^{\frac{2}{3}}h^{\frac{4}{3}}}} \tag{2.22}$$

where f_{snap} represents the static collapse load in the presence of only transverse (no in-plane) loading. The static collapse load is seen to be a function of only the undeformed spring length, the 'shell' depth, and the spring stiffness. Eq (2.19) is plotted in Figure 3.1 on page 3-2.

2.2.3 Dynamic Collapse Load. Calculation of the dynamic collapse load must include two quantities ignored in the calculation of the static collapse load: mass (inertia) and the load function $f(t)$. Eq (2.18) is the differential equation representing the motion in the w direction. In an attempt to find a closed form solution, we restrict the motion to the w axis, i.e. $u = v = 0$, and we exclude damping. Under these conditions, Eq (2.18) becomes

$$m\ddot{w} + 2kw + k\left\{b(d-w)\left(\frac{b_3 + l_4}{b_3 b_4}\right) - 2d\right\} = f_w \tag{2.23}$$

But when $u = v = 0, b_3 = b_4$ and Eq (2.23) becomes

$$m\ddot{w} + 2kw + k\left\{b(d-w)\left(\frac{2}{b_3}\right) - 2d\right\} = f_w$$

which simplifies to

$$m\ddot{w} + 2k(d-w)\left(\frac{b}{b_3} - 1\right) = f_w$$

Eq (A.1) gives us b_3 which, with $u = v = 0$ is

$$b_3 = \sqrt{h^2 + (d-w)^2}$$

Substitution yields

$$m\ddot{w} + 2k(d-w)\left(\frac{b}{\sqrt{h^2 + (d-w)^2}} - 1\right) = f_w \tag{2.24}$$

Despite the simplification of confining the motion to the z axis, Eq (2.24) is a non-linear second order differential equation whose closed form solution is not obvious and likely exists only for certain parameters. Mathematical theorems, such as the uniqueness and existence theorem (5:24–25) reveal the conditions for which solutions are guaranteed to exist, but do not *produce* those solutions. For describing the general motion of the mass, numerical solutions may be had more quickly than analytical ones. Furthermore, under cyclic loading, the dynamic collapse load loses its meaning in that there is no 'threshold value' at which it may be said instability (collapse) is sure to occur (see Section 3.4, page 3-11).

2.2.4 A Checking Mechanism. It would be desirable to have an 'independent' check that the computer program is converging to a reasonable solution for each time increment Δt. Toward this goal, a checking mechanism is incorporated into the model to monitor the energy-balance for the no damping case. The idea for using energy as a check comes from Kounadis' work in studying chaoslike phenomena of suddenly load structures (14:302).

The check is performed as follows:

1. The cumulative error, E , the integrated work performed, W , and the cumulative percent error, E_{pct} are set equal to zero:

$$E = W = E_{pct} = 0 \tag{2.25}$$

2. At the end of the ith time step, the change in kinetic energy, δT_i , potential energy, δV_i , and work performed by the external force, δW_i (using the average force of the current and previous time step) are calculated:

$$\delta T_i = \frac{1}{2} m \left[\left(\sum_{j=1}^{3} \dot{x}_j^2 \right)_i - \left(\sum_{j=1}^{3} \dot{x}_j^2 \right)_{i-1} \right] \tag{2.26}$$

$$\delta V_i = \frac{1}{2} \left[\sum_{l=1}^{4} k_l (b_l - b)_i^2 - \sum_{l=1}^{4} k_l (b_l - b)_{i-1}^2 \right] \tag{2.27}$$

$$\delta W_i = \frac{1}{2} \sum_{j=1}^{3} \left\{ \left[(f_j)_i + (f_j)_{i-1} \right] \left[(x_j)_i - (x_j)_{i-1} \right] \right\} \tag{2.28}$$

where the k_l are the spring stiffnesses for each of the four linear springs, the b_l are the deformed spring lengths, b is the undeformed spring length (equal for all springs), m is the mass, and the j index refers to the component directions, e.g. $\dot{x}_2 = \dot{v}$ and $f_3 = f_w$.

3. Next, the error for the ith time step, δE_i , and is calculated:

$$\delta E_i = |\delta W_i - \delta T_i - \delta V_i| \tag{2.29}$$

4. The cumulative error and cumulative work performed may then be calculated, yielding the cumulative percent error:

$$E_i = E_{i-1} + \delta E_i$$

$$W_i = W_{i-1} + \delta W_i$$
$$(E_{pct})_i = 100 \frac{E_i}{W_i} \tag{2.30}$$

5. Finally, an rms value of error is calculated as follows:

$$(e_{rms})_i = \sqrt{\frac{\sum_{n=1}^{i} (E_{pct})_n^2}{i}} \tag{2.31}$$

At the end of each time step, e_{rms} is compared to a user defined maximum (typical values are employed in Section 3.4). If the maximum error is exceeded, the program notifies the user and terminates, otherwise, another time step is taken and the error checked beginning with step 2. The FORTRAN implementation of the energy balance scheme is provided in Appendix C.

2.2.5 The Integration Scheme. (31:190–193)

An iterative procedure is used to solve the nonlinear equations of motion. This predictor-corrector method involves predicting the outcome for a step in time, then applying an implicit correcting formula to improve the result. The subsequent result is then used as the prediction, the corrector is applied, and the process continues. This particular algorithm was chosen for several reasons: (1) the method is specifically designed for second-order ordinary differential equations, (2) it is an implicit and unconditionally stable algorithm, and (3) with only three degrees of freedom, employing a more complex matrix-oriented scheme is not necessary or practical — the three closed-form solutions for the accelerations are easily calculated by the computer, eliminating the need for iterating to solve for accelerations (as in the beta-m method). The algorithm will be described for the w coordinate, though calculations for the u and v coordinates are identical.

For the first iteration, the velocity is estimated at the end of the first time step:

$$\dot{w}_1 = \dot{w}_0 + \ddot{w}_0 \Delta t_0 \tag{2.32}$$

Where $\dot{w}_0$ and $\ddot{w}_0$ are the initial velocity and acceleration in the w direction. The displacement w is then predicted based upon the predicted velocity:

$$w_1 = R_w + \frac{1}{2}\dot{w}_1 \Delta t_0 \tag{2.33}$$

Where $R_w = w_0 + \frac{1}{2}\dot{w}_0 \Delta t$, with w_0 being the initial displacement. The closed form solution for the acceleration, shown in Eq (2.18), is then used to calculate $\ddot{w}$.

For subsequent iterations i on time step j, $j > 1$, the procedure is similar. First, velocity is predicted:

$$(\dot{w}_j)_i = (Q_w)_{j-1} + \frac{1}{2}(\ddot{w}_j)_{i-1} \Delta t_{j-1} \tag{2.34}$$

Where $(Q_w)_{j-1} = \dot{w}_{j-1} + \frac{1}{2}\ddot{w}_{j-1}\Delta t_{j-1}$. Then, displacement is predicted based upon the predicted velocity:

$$(w_j)_i = (R_w)_{j-1} + \frac{1}{2}(\dot{w}_j)_i \Delta t_{j-1} \tag{2.35}$$

Convergence is checked for by comparing the difference between the displacement calculated for the current iteration and the displacement calculated in the previous iteration. If the difference is less than some arbitrary user-defined ϵ, the iteration is successful. If not, a new $\ddot{w}$ is calculated and a new iteration is begun. As in the DSHELL finite element model, MSHELL uses an averaging scheme to check for convergence, such that, at the ith iteration,

$$\frac{\left| \left(\sqrt{\sum_{j=1}^{3} (x_j)^2} \right)_i - \left(\sqrt{\sum_{j=1}^{3} (x_j)^2} \right)_{i-1} \right|}{\left(\sqrt{\sum_{j=1}^{3} (x_j)^2} \right)_i} \leq \epsilon \tag{2.36}$$

must be satisfied for convergence to be deemed successful (30:2-38).

Like the beta-m method, this is a single-step method, allowing change of the time step during a computer run. The FORTRAN implementation of this method is provided as Appendix B.

2.9 *Chaos*

There are three classic types of dynamical motion:

1. Equilibrium
2. Periodic motion or a limit cycle
3. Quasiperiodic motion

In phase space, the equilibrium state is associated with a point, the periodic motion with a closed curve, and the quasiperiodic motion with a surface in three-dimensional phase space. These states are called *attractors*, since, with damping, the dynamical system's motion tends to decay to one of these three states. Chaotic behavior, however, involves yet another attractor called a ***strange attractor***. Unlike the classic attractors, this attractor is not associated with a classical geometric object in phase space, but a new geometric object called the *fractal set*. In three-dimensional phase space, the fractal set of a strange attractor looks like "...a collection of an infinite set of sheets or parallel surfaces, some of which are separated by distances that approach the infinitesimal (17:23)."

There are several useful graphical tools for the analysis of nonlinear systems. Consider a linear[4], one degree of freedom, forced spring-mass system (31:48–49). The motion includes the steady state response at the frequency of the forcing function, Ω , superimposed on the transient response at the natural frequency of the system, $\omega = \sqrt{k/m}$. The second order differential equation of motion for this system is

$$m\ddot{x} + kx = f \sin \omega t \tag{2.37}$$

and its solution for $x(0) = \dot{x}(0) = 0$ is

$$x(t) = \frac{f/m}{\omega^2 - \Omega^2} \left(\sin \Omega t - \frac{\Omega}{\omega} \sin \omega t \right) \tag{2.38}$$

[4] A linear system is used here for illustration as the closed form solution of the differential equation is immediately available.

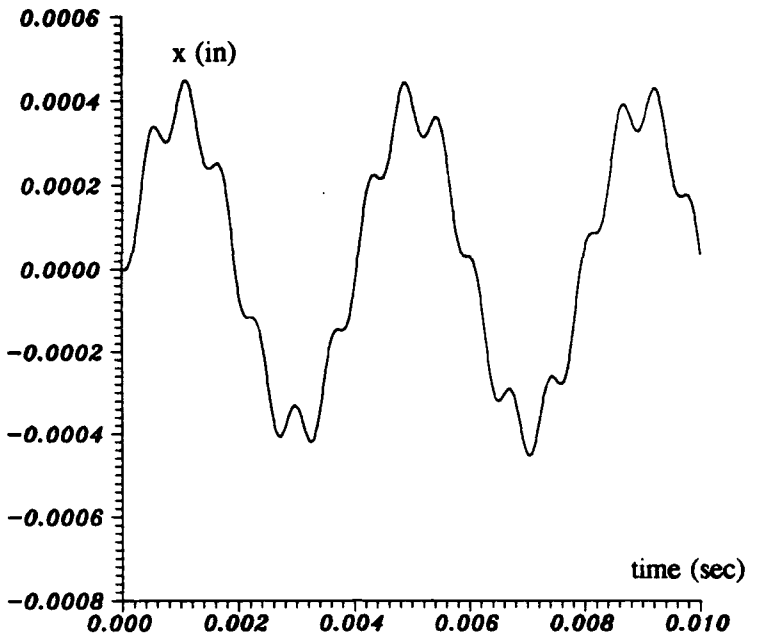

Figure 2.5. Displacement vs. time for forced, undamped linear vibration

The motion versus time for a particular choice of k, m, f, and Ω is depicted in Figure 2.5. The *phase diagram* plots velocity versus displacement for a dynamical degree of freedom. The path traced by the function is referred to as the *trajectory*. The phase diagram for the example system is shown in Figure 2.6.

The *Poincaré section* plots points which represent snapshots in time of the phase diagram. The phase diagram is sampled at a particular frequency (usually the frequency of the forcing function) and the sampled points form the Poincaré section. The Poincaré map is also referred to as a *surface of section*, because it may be generated by sampling the displacement and velocity as the object crosses a plane or surface in space. Among other things, the Poincaré section indicates resonances between the forcing function and the dynamical system's response. The Poincaré map for the example system is shown in Figure 2.7. The sampling rate is the frequency of the forcing function, with a phase angle of zero.

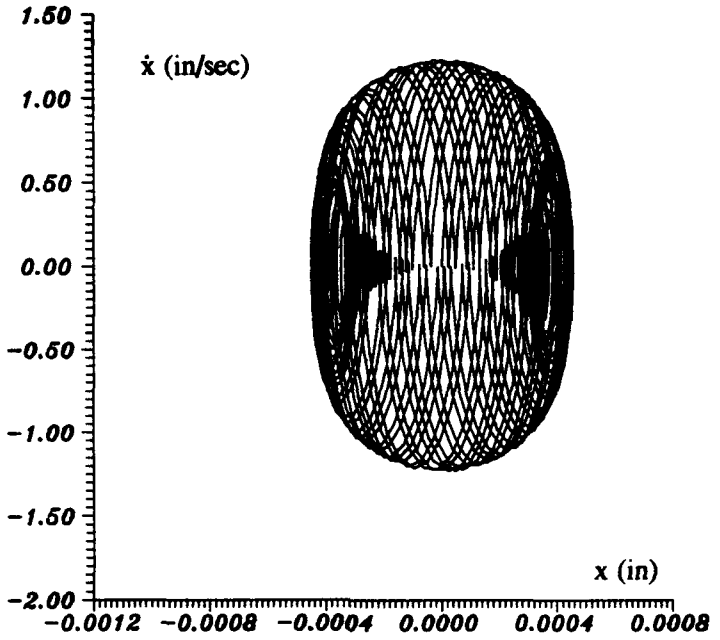

Figure 2.6. Phase diagram for forced, undamped linear vibration

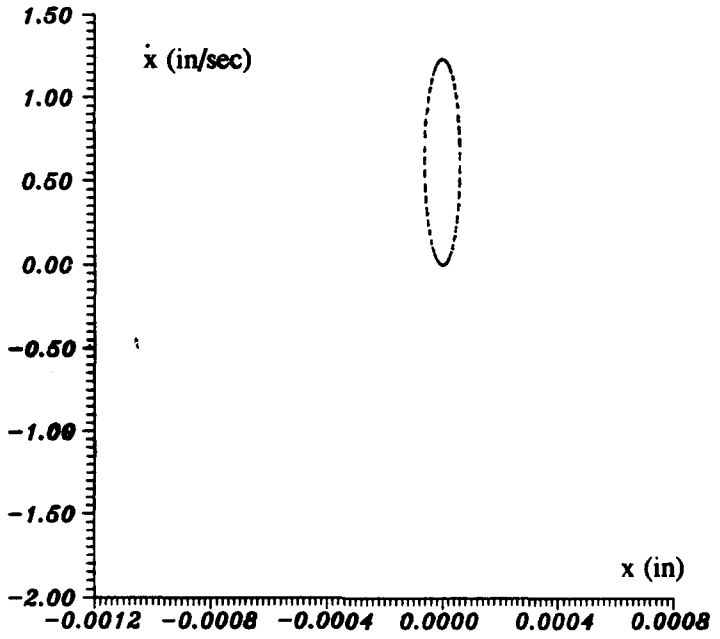

Figure 2.7. Poincaré section for forced, undamped linear vibration

The *Fourier transform* may be used to determine the *power spectrum* of a particular motion. The power spectrum relates frequencies of motion to the energy the frequencies contain. Power spectra with discrete peaks of energy indicate non-chaotic behavior, while broad-banded 'noise-like' spectra may indicate chaotic behavior. Near the onset of chaos, the discrete peaks are absorbed into a more continuous distribution of frequencies. With fully chaotic behavior, the continuous spectrum may dominate the discrete spikes (17:148). The *Fast Fourier Transform* (FFT) is used in this research. It has the advantage of needing on the order of $N \log_2 N$ operations as compared to N^2 operations for the *Discrete Fourier Transform* (DFT), where N is the number of sampled data points (11:766). In the DFT (and hence the FFT, which is but a special algorithm for calculating the DFT) the sampled data set is represented by a set of Fourier coefficients $A_r(\omega)$

$$A_r(\omega) = \sum_{k=0}^{N-1} X_k \exp(-2\pi i r k/N), \qquad r = 0, 1, \ldots, N-1 \tag{2.39}$$

where X_k is the sampled data set (in this case, the displacement samples), and $i = \sqrt{-1}$. The coefficients $A_r(\omega)$ are generally complex, so it is useful to define a real-valued function called the *power spectrum*, $S(\omega) = ||A_r(\omega)||^2$ (2:31). The FFT is used to generate Figure 2.8, which reveals the forcing frequency, $f_\Omega = 250$ Hz, and the system's natural frequency, $f_\omega = 1597$ Hz. The amplitude information reveals how relatively little excitation is caused when the forcing frequency is far from the system's natural frequency. A key rule of thumb in taking data from the time domain to the frequency domain is that the sampling rate should be at least twice that of the highest frequency of interest. In this research, the time steps used are less than 0.0001 seconds, corresponding to a sampling rate of 10 kHz, hence capturing frequencies below 5 kHz. And for many plots, the sampling rate is much higher.

The *bifurcation diagram* plots velocity versus some other system parameter (such as the amplitude of the applied load). The points are sampled as in the Poincaré section. Hence each vertical slice of the bifurcation diagram may be thought of as a collapsed Poincaré section for a particular

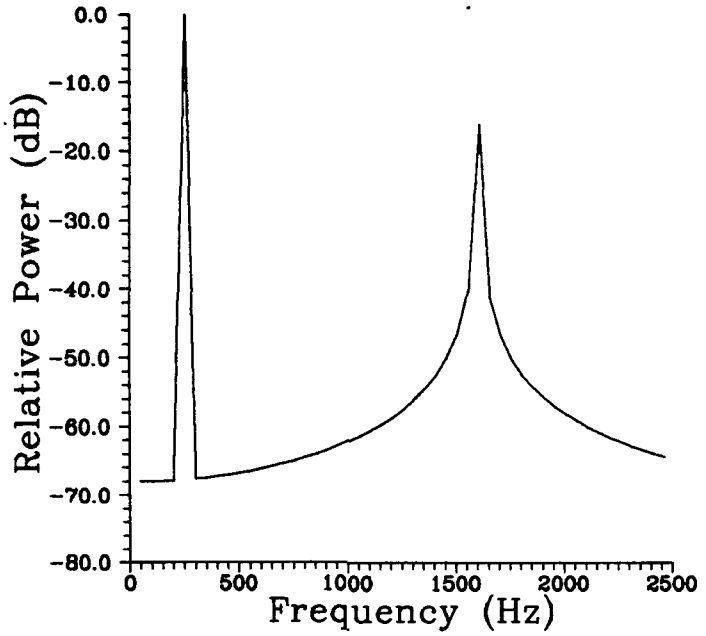

Figure 2.8. Relative power vs. frequency for forced, undamped linear vibration

load condition. The bifurcation diagram depicts the solution(s) to the nonlinear differential equation given a particular forcing function. In generating the bifurcation diagrams, care must be taken to discard early transient motion (17:130). Figure 3.12 on page 3-10 is a bifurcation diagram.

Two specific types of bifurcation are seen in the current research. *Period doubling*, also called the ***flip bifurcation*** occurs when different oscillatory motions of the same frequency, ω, combine in such a fashion as to repeat at a frequency of $\omega/2$ (2:72). When this happens, the closed orbit (in phase space) representing the fundamental frequency loses its stability and is replaced by another (stable) closed orbit whose period is twice that of the original (29:127). The flip bifurcation is peculiar to cycles and, unlike the fold bifurcation, has no correspondence for equilibria (29:127).

The ***fold bifurcation***, also called a saddle-node bifurcation, is exemplified in the snap-buckling of a support arch (or shell) under vertical load (29:256). The fold bifurcation is a structurally stable bifurcation, arising when a pair of equilibria exist -- one unstable and the other attracting (29:256).

2.4 Selection of Time Step, Δt

Choosing an appropriate time step, Δt , for a given dynamic nonlinear problem is both very important and very difficult. Both the behavior of the forcing function, $f(t)$, and the behavior (response) of the dynamical system acted upon by $f(t)$ must be captured (15:550). Depending on the integration technique, the choice of Δt may determine the stability of the integrating scheme. Even in those cases where unconditionally stable integrating techniques are used (such as in the present research), numerical accuracy is not assured—the algorithm may always converge, but it may converge to a solution not of the desired accuracy. Unfortunately, decreasing the time step does not guarantee an improvement in accuracy. There is a minimum Δt below which accuracy is compromised due to increasing the number of calculations performed over the duration of the computer run (round-off error). In addition, practical considerations, such as limits on computer time, drive the analyst toward using the largest possible time step that gives acceptable results. The DSHELL program executes over 10,000 lines of code for a single iteration of a single time step (27), and it is not uncommon for 5 or more iterations to be required for convergence in a time step. For most of the runs done in the present research, an extremely small convergence tolerance of (10^{-10}) percent was used. This was done in an effort to eliminate cumulative error due to poor accuracy in the convergence as a source of instability. Happily, the choice of such a small tolerance does not significantly increase the number of iterations required for convergence — the choice of Δt has a much more pronounced effect.

Many investigators have suggested various 'rules of thumb' for choosing an appropriate Δt. Table 2.2 lists some of these rules and their sources. In Table 2.2, τ_1 is the period associated with the first fundamental frequency of vibration, τ_{max} is the period associated with the highest frequency of interest, and τ represents *the* frequency of oscillation of a single degree of freedom system. In addition to these, Almroth and Brogan (1:6-32–6-37) offer several methods with the caveat that trial and error may be required following the first choice for Δt. Almroth, Brogan,

Technique	Source
$\Delta t_{max} = \tau_1/120$ for 10% accuracy or better	Low (15:556)
$\Delta t_{max} = \tau_{max}/20$ or less for nonlinear problems	Cook, et al. (8:407)
$\Delta t_{max} = \tau/12$	Katona and Zienkiewicz (13:1356)

Table 2.2. Techniques for choosing Δt

and Cook note well that modification of the initial choice for Δt may be required, particularly in the nonlinear case. Employing any of these 'rules of thumb' for choosing an appropriate time step involves having *a priori* knowledge of how the system behaves.

What makes the choice of time step particularly difficult is the physical behavior of the nonlinear problem. For example, the inertial forces during and after collapse (snapping) may be much larger than before collapse or during steady-state oscillation. An eigenvalue analysis yields clues as to the frequencies of interest, but only in the neighborhood of the undeformed geometry. The eigenvalues (and hence the natural frequencies) change as the object deforms. In the present research, a Δt suitable for prebuckling or steady-state response was unsuitable for postbuckling behavior. In studies of the laminated composite arch, the postbuckled deformed geometry was seen to change radically over just one step in time, casting doubt on whether the geometry found was correct or just another (incorrect) geometry satisfying the energy balance equations of the structure.

2.5 Post-processing Capability

As part of this research, two FORTRAN routines were written to facilitate post-processing of the DSHELL output.

Since Dennis (9) authored the SHELL code in 1988, users of the code have used various means of analyzing the results. However, no full-featured post-processing capability was available. Minor changes have been made to the code at various times to allow plotting programs, such

as GRAPHER™, to present limited amounts of data in a more easily evaluated form, but no means have been available to view the entire deformed structure and the associated displacements, velocities, accelerations, strains, and stresses in a comprehensive way. For this reason, one goal of this research was to incorporate such a capability.

2.5.1 Subroutine UNV. The FORTRAN routine UNV allows the user of DSHELL to capture most of the output generated by the program. UNV generates a file[5] in a format SDRC's I-DEAS[6] computer program can read. The extensive post-processing capabilities of I-DEAS allow the user to view the data generated by DSHELL in a graphical way. The user may view the structure in perspective views and see the actual deformed geometry. The user may view contour plots (in color) of various quantities (velocity, stress, rotational acceleration, etc.) superimposed on the deformed geometry.

I-DEAS also gives the user the ability to plot the data from the DSHELL run and, if the plotting style of another plotter is preferred, I-DEAS can output the data in tabular (spreadsheet) form for use by another plotting program of the user's choice.

The user of UNV may specify any or all of the following data to be captured:

- nodal displacements (including rotations)
- nodal velocities
- nodal accelerations
- elemental stresses
- elemental strains

If the particular problem can be represented using one-fourth of a bilaterally symmetric structure, the user may choose the symmetry option when running UNV. Choosing this option

[5]SDRC refers to this as a 'universal' file.
[6]I-DEAS and SDRC are trademarks of Structural Dynamics Research Corporation.

causes UNV to reflect the data from the article into three adjacent quadrants, allowing the user to 'see' a representation of the entire article. *This option is only successful when Node Number 1 resides at the intersection of the two axes of symmetry.*

UNV automatically chooses either rectangular Cartesian or cylindrical coordinates depending on the model chosen. If an arch or shell is modeled, UNV will generate data in cylindrical coordinates. Choosing a plate model causes UNV to generate results in rectangular Cartesian coordinates. In any case, the graphics presented by I-DEAS will depict a rectangular system in the corner of the terminal screen. For cylindrical coordinates, the axis directions on the screen correspond to the article's coordinate system as follows:

- the $+x$ direction corresponds to $+r$ $(-w)$
- the $+y$ direction corresponds to $+\theta$ $(+s)$
- the $+z$ direction corresponds to $+z$ $(+u)$

In DSHELL, w displacements for the mid-side nodes are implied, not calculated. In order to plot the displacements, UNV generates a cubic curve fit that matches the slope ($w_{,1}$ or $w_{,2}$) at the corner nodes and has the appropriate calculated u or v displacement of the mid-side node (depending on the direction of interpolation).

2.5.2 Subroutine UMODAL. The FORTRAN routine UMODAL, allows the user to view, using I-DEAS, the physical mode shapes associated with the eigenvalues calculated by DSHELL. DSHELL calculates the displacements and rotations at each element corner node, but UMODAL captures only the displacements, not the rotations.

2.5.3 The Input Deck. Use of the post-processing features requires inserting one card into the input deck. It becomes the first card, and is of the form

```
MAKE_UNV,ISYMM,U_LIMIT,MB_MAX,NO_PRINT,U_DISP,U_VEL,U_ACC,U_STRESS,U_STRAIN
```

where the values of the variables and their functions are described in Table 2.3.

Variable	Data Type	Function
MAKE_UNV	*integer*	= 0, do not create universal file = 1, create universal file
ISYMM	*integer*	= 0, do not use symmetry = 1, use symmetry by reflecting the model about Node 1 assuming bilateral symmetry
U_LIMIT	*integer*	= 0, do not limit the size of the universal file = 1, limit the size of the universal file to MB_MAX megabytes
MB_MAX	*integer*	(see U_LIMIT)
NO_PRINT	*integer*	= 0, print stress data to output file[Note] = 1, do not print stress data to output file
U_DISP	*integer*	= 0, do not capture nodal displacements and rotations = 1, capture nodal displacements and rotations
U_VEL	*integer*	= 0, do not capture nodal velocities = 1, capture nodal velocities
U_ACC	*integer*	= 0, do not capture nodal accelerations = 1, capture nodal accelerations
U_STRESS	*integer*	= 0, do not capture elemental stresses = 1, capture elemental stresses[Note]
U_STRAIN	*integer*	= 0, do not capture elemental strains = 1, capture elemental strains
Note: If the value of **U_STRESS** is 1, then the user must select **NSTRES** to equal the total number of elements and **ISTRES(I)** must contain each and every element number. This will generate very large output files unless **NO_PRINT** is set to one.		

Table 2.3. Variable list for data input card for use with postprocessor

III. MSHELL: *THE SIMPLIFIED SHELL MODEL*

The MSHELL model was generated with the goal of getting insight into some of the phenomena observed through the DSHELL finite element code. The MSHELL code is only a small fraction of the size of DSHELL, and run times are commensurately smaller. Through the use of MSHELL, thousands of oscillations may be observed in a few minutes of computer time, whereas with DSHELL, ten oscillations of the vibrating shell may take several days of computer time to generate. The MSHELL model by no means has the fidelity of the finite element model, but many of the fundamental characteristics of shell behavior are modeled (see page 2-8).

3.1 The Model Parameters

Parameters for the model are chosen to match the geometry, linear fundamental natural frequency, and static buckling load of the cross-ply laminated shell used in the present research. The stiffness of springs 3 and 4 determine the static collapse load (with w displacement alone) of the MSHELL model. The constants of springs 1 and 2 were empirically chosen to match the ratio of in-plane to transverse amplitudes seen in edge nodes of the composite shell subjected to a sudden load. The parameters are listed in Table 3.1. These parameters yield the linear natural frequencies

k_i, lbs/in							
1	2	3	4	b, in	h, in	d, in	m, slugs
39,235	39,235	78,470	78,470	5.9377	5.7532	1.4686	$1.5588(10^{-2})$

Table 3.1. Parameters for simple shell-like model

shown in Table 3.2. The first mode is seen to be the transverse vibration, and the second the in-plane vibration. The load versus displacement described by Eq (2.19) for this model is depicted in Figure 3.1.

	ω	f (Hz)	τ (sec)	Mode Shape
Mode 1	3173	505	0.0020	$\begin{pmatrix} 0 & 0 & w \end{pmatrix}$
Mode 2	3886	618	0.0016	$\begin{pmatrix} u & v & 0 \end{pmatrix}$

Table 3.2. Linearized behavior of simple shell-like model

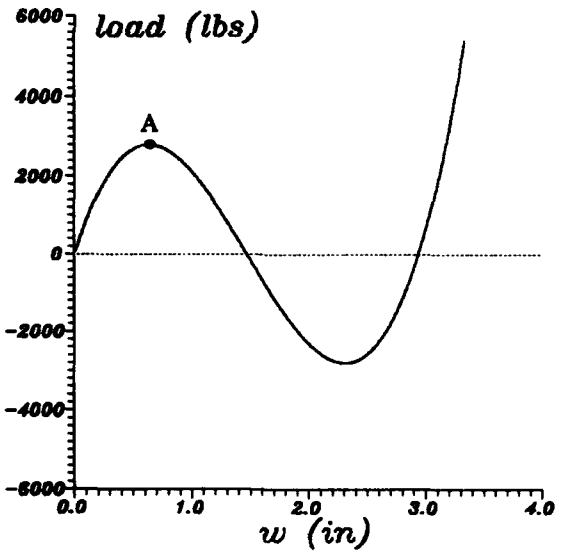

Figure 3.1. Load vs. displacement for simple shell-like model. The static snap load is depicted at point 'A'.

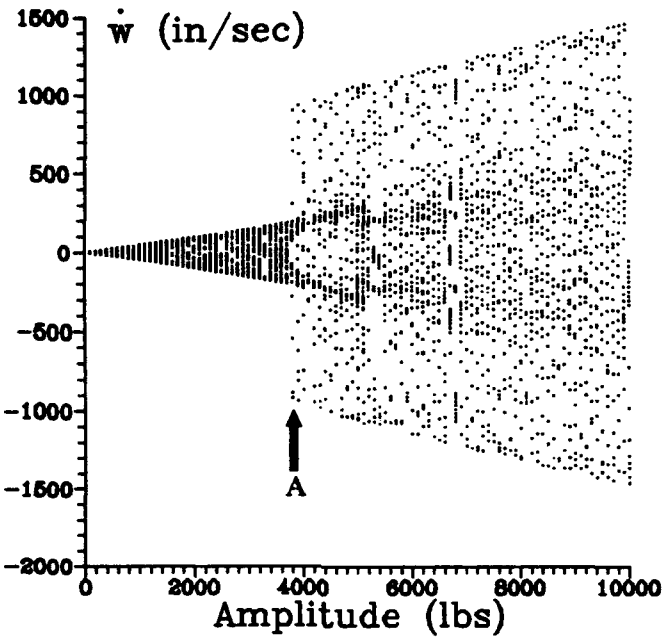

Figure 3.2. Bifurcation plot for MSHELL model, sudden loading, $r = 10^6$ lbs/sec, depicting collapse load at A

3.2 Response to Sudden Loading

The response of the MSHELL model to sudden loading was observed at two different load rates, r , both of which result in collapse (buckling) of the model. The load is applied in a highly eccentric fashion in order to excite in-plane as well transverse motion. Figure 3.2 is the bifurcation diagram for the suddenly loaded model. This plot is generated by forming the Poincaré map at each amplitude and collapsing it in the displacement direction. In other words, each vertical slice of the bifurcation diagram is a Poincaré map collapsed in the x direction. The arrow at point A indicates the onset of collapse behavior.

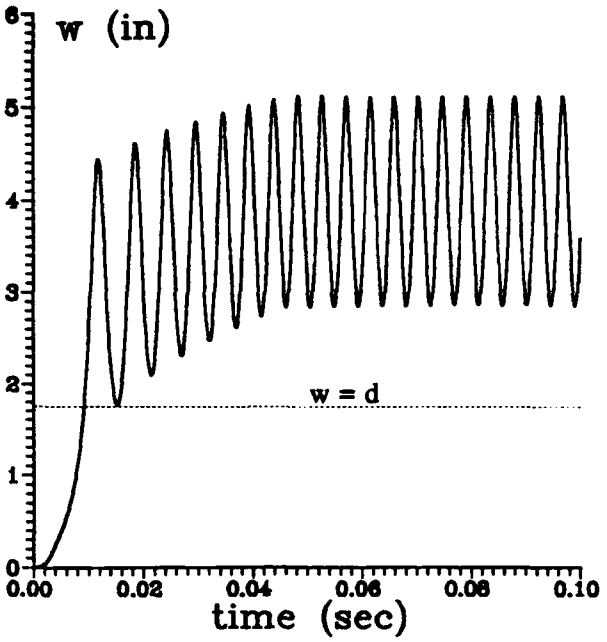

Figure 3.3. MSHELL model w displacement vs. time for step load of 46,000 lbs applied at 10^6 lbs/sec

In the first case, the model is loaded at a rate[1] of $r = 10^6$ lbs/sec:

$$\vec{\mathbf{f}} = \frac{1}{\sqrt{3}} \begin{bmatrix} 1 \\ 1 \\ 1 \end{bmatrix} f(t), \qquad \text{where } f(t) = \begin{cases} 10^6 t, & t < 46,000/10^6 \\ 46,000, & t \geq 46,000/10^6 \end{cases} \tag{3.1}$$

Here $\vec{\mathbf{f}}$ is the load function. Under these conditions the model collapses and assumes a steady state oscillation with $w > d$. The displacement versus time plot may be seen in Figure 3.3. In phase space (Figure 3.4), this undamped system is seen to rapidly converge to a fixed orbit — a purely periodic motion. The frequency response generated by these conditions is depicted in Figure 3.5, with the energy peak at 228 Hz. The subsequent peaks represent the second and third harmonics of this fundamental nonlinear frequency of vibration.

[1]This load rate is chosen because it is frequently used in the finite element model analyses.

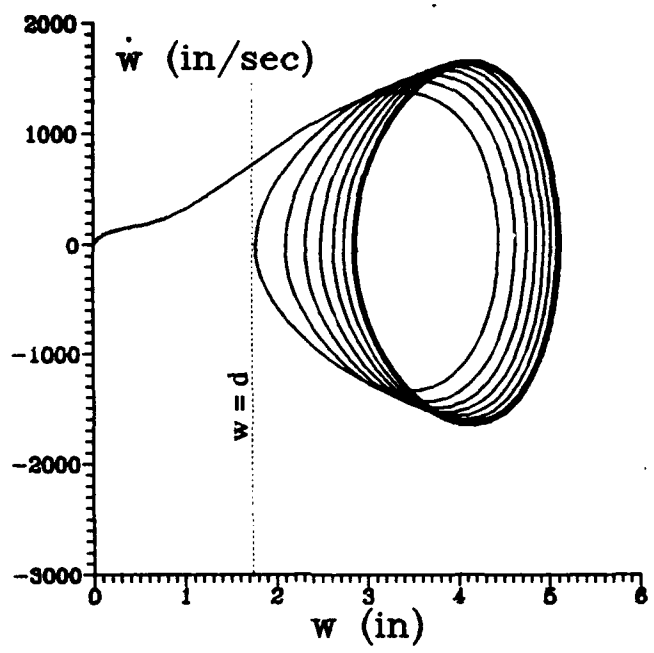

Figure 3.4. MSHELL model w phase diagram for step load of 46,000 lbs applied at 10^6 lbs/sec

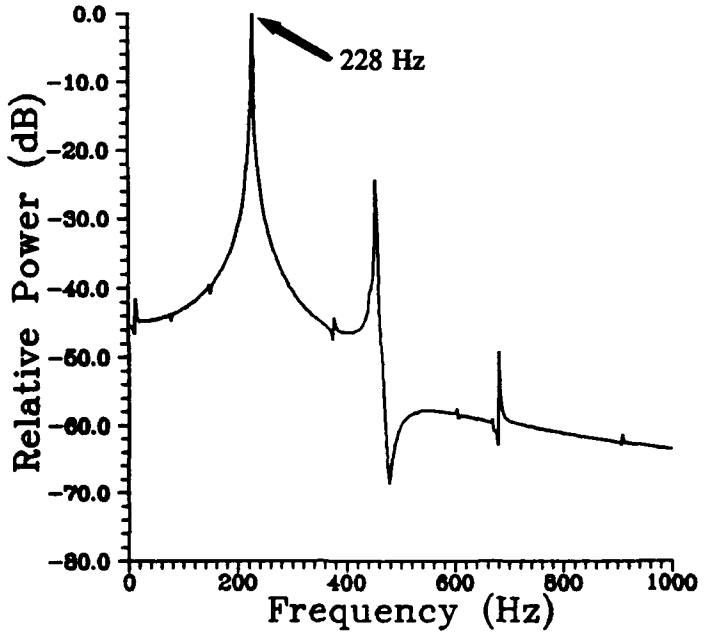

Figure 3.5. MSHELL model frequency response for step load of 46,000 lbs applied at 10^6 lbs/sec

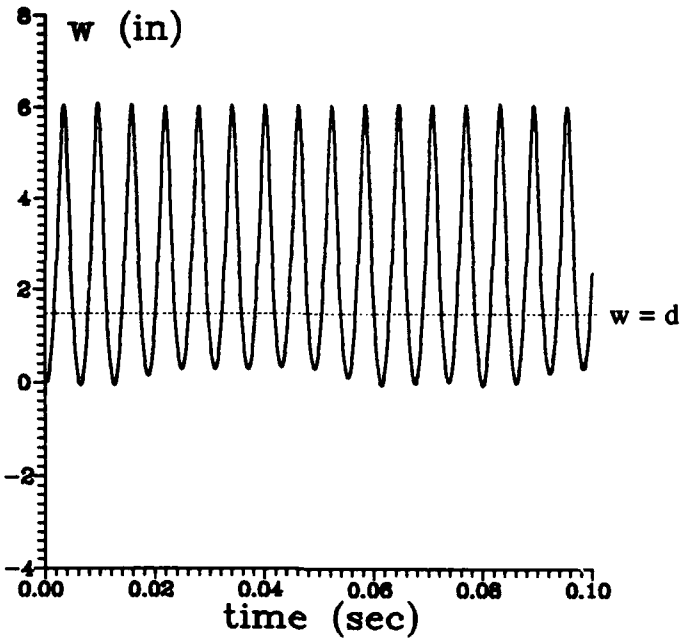

Figure 3.6. MSHELL model w displacement vs. time for step load of 46,000 lbs applied at 10^8 lbs/sec

In the next case, the model is suddenly loaded at a rate $r = 10^8$ lbs/sec in an effort to generate snap-through in both directions (snap-through followed by snap-through in the opposite sense). At this higher load rate, the mass does snap through and then rebounds completely back through the $w = d$ plane. Subsequent oscillations continue to cross this plane (see Figures 3.6 and 3.7). The larger amplitude leads to a lower nonlinear frequency of oscillation, and this is depicted in Figure 3.8. The bifurcation plot for this load rate (not shown) looks virtually identical to that of Figure 3.2, except that the onset of buckling occurs at a lower load.

3.3 Response to Sinusoidal Loading

To simulate the behavior of a node in the DSHELL finite element model, in which every unrestrained node pulls on every other node, the MSHELL model is loaded sinusoidally. The

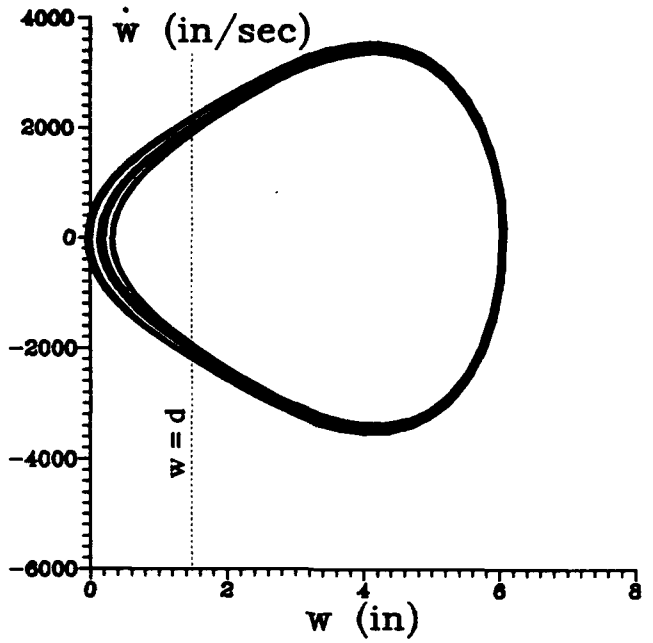

Figure 3.7. MSHELL model w phase diagram for step load of 46,000 lbs applied at 10^8 lbs/sec

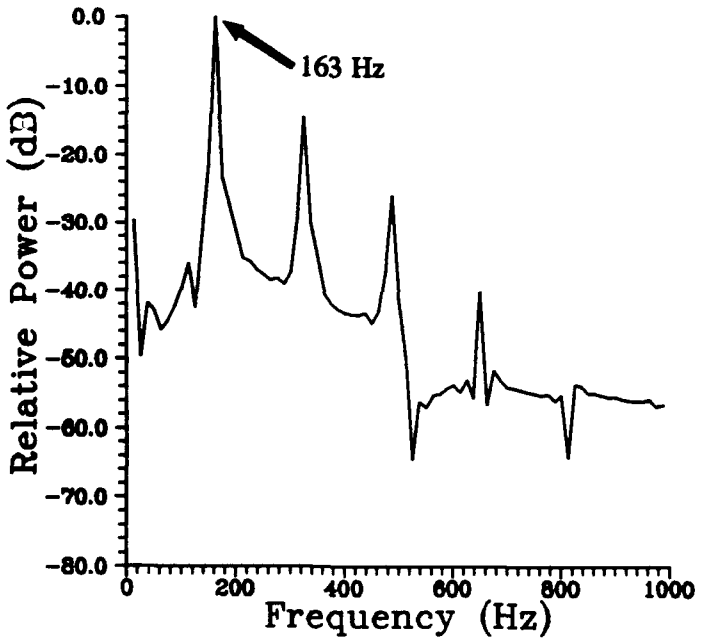

Figure 3.8. MSHELL model frequency response for step load of 46,000 lbs applied at 10^8 lbs/sec

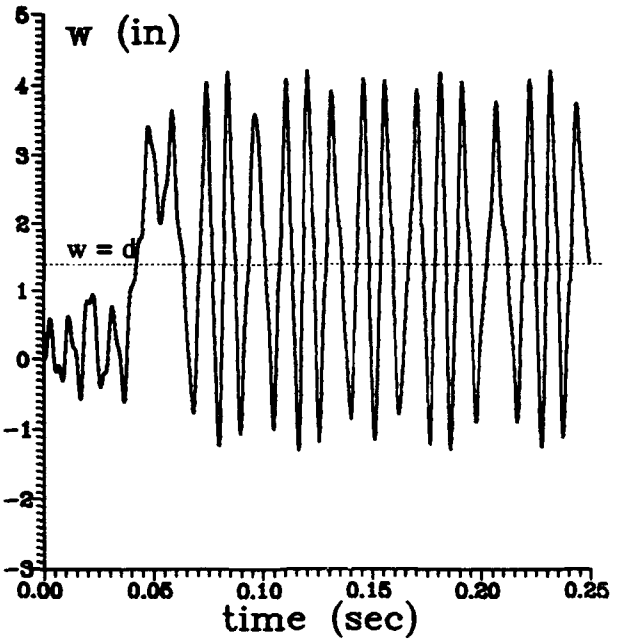

Figure 3.9. MSHELL model w displacement vs. time for sinusoidal load of $10,000\sin(1571t)$ lbs

loading for this case is

$$\vec{\mathbf{f}} = \frac{1}{\sqrt{3}} \begin{bmatrix} 1 \\ 1 \\ 1 \end{bmatrix} 10,000\sin(1571\,t) \tag{3.2}$$

The circular frequency of 1571 s^{-1} corresponds to $f = 250$ Hz. This frequency is used because it approximates the nonlinear fundamental frequency of vibration observed in the finite element model subjected to a sudden load below the buckling load (see Figure 4.13 on page 4-12).

Figure 3.9 plots the w displacement of the mass versus time. The model does not buckle until the fifth cycle, after which snap through (in both directions) occurs. Though not shown in Figure 3.9, as time increases the model is seen to have periods of oscillation during which the mass remains on the prebuckled side of the $w = d$ plane for several cycles, then resumes the buckled motion. These regions are seen in the phase diagram (Figure 3.10) as small orbits near the value

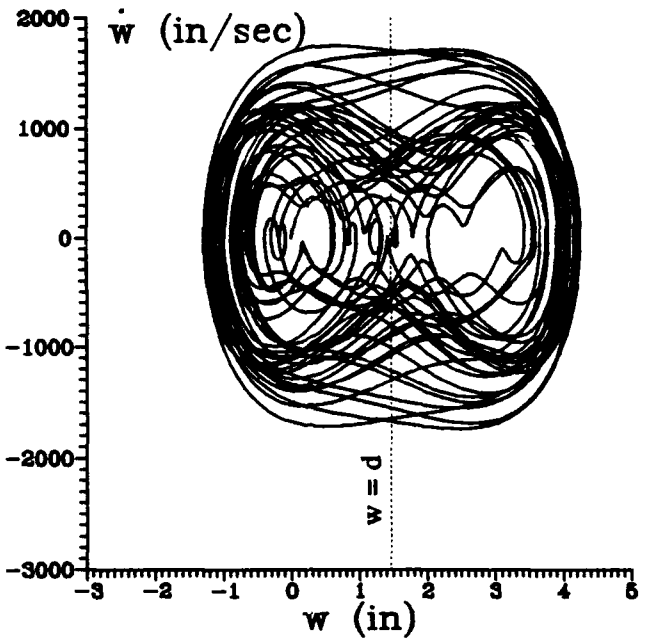

Figure 3.10. MSHELL model w phase diagram for sinusoidal load of $10,000\sin(1571t)$ lbs

$w = 0$ (Figure 3.10 represents a much greater time span than Figure 3.9). The frequency response of this model (Figure 3.11) shows the broad-banded response associated with chaos (17:148).

A bifurcation plot, Figure 3.12, was generated for the sinusoidal loading case. In the region at A, the orbits suddenly enlarge — the result of a flip bifurcation. The origin of the 'hole' at B is not yet understood, but the points C represent collapse behavior.

A Poincaré map of the case with amplitude of 10,000 lbs is shown in Figure 3.13. The Fourier transform indicates chaotic motion, though the Poincaré map shows no chaotic attractor. This is due to the lack of damping. "If a system does not have sufficient damping, the chaotic attractor will tend to fill up a section of phase space uniformly and the Cantor set structure, which is characteristic of strange attractors, will not be evident (17:134)."

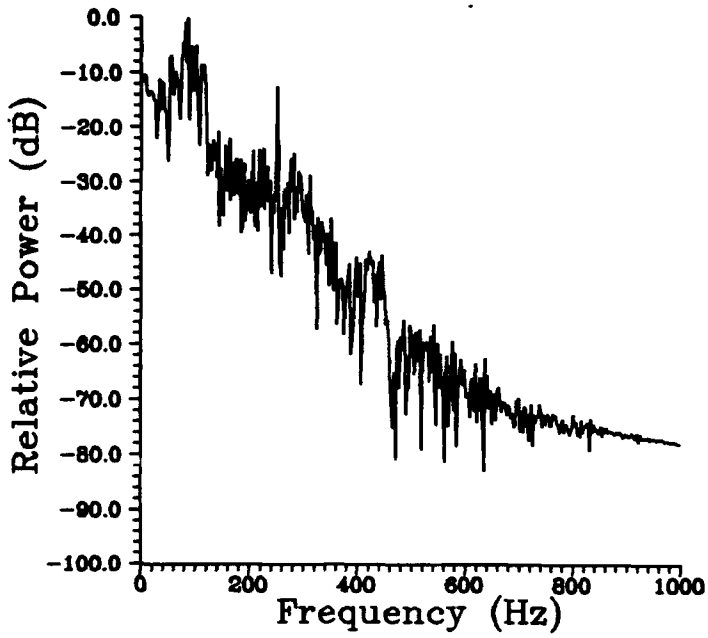

Figure 3.11. MSHELL model frequency response for sinusoidal load of $10,000 \sin(1571t)$ lbs indicating chaotic behavior

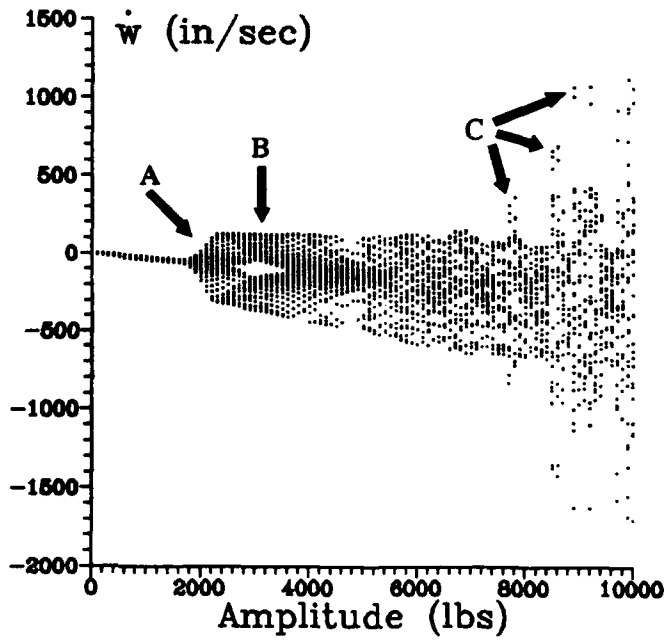

Figure 3.12. Bifurcation plot of MSHELL model, sinusoidal loading

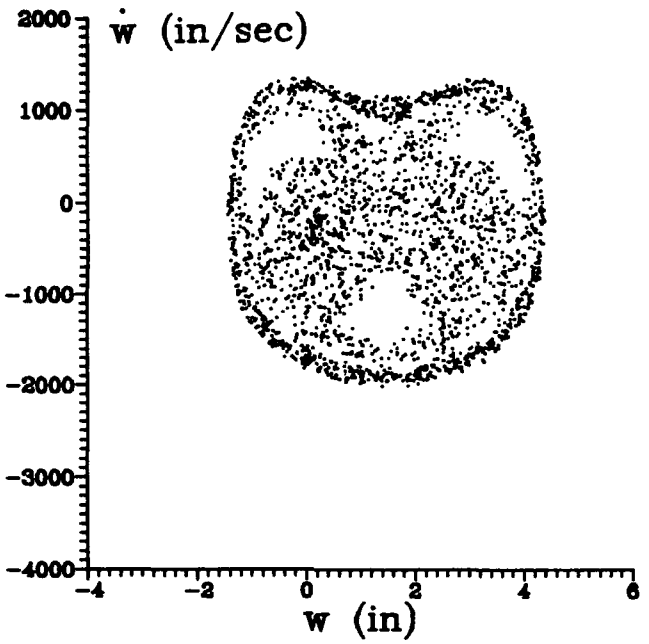

Figure 3.13. Poincaré map for sinusoidal loading, amplitude of 10,000 lbs

3.4 Methods for Choosing Time Step, Δt

Using the MSHELL model, a series of simulations was run to find an empirical relationship between the system dynamical behavior and the required time step, Δt. Two cases were run using the MSHELL model. In the first case, the MSHELL model, with parameters as in Table 3.1 on page 3-1, is loaded sinusoidally with load $\vec{\mathbf{f}}$ given by

$$\vec{\mathbf{f}} = \frac{1}{\sqrt{3}} \begin{bmatrix} 1 \\ 1 \\ 1 \end{bmatrix} f_0 \sin \Omega t \tag{3.3}$$

with $\Omega = 1571$ radians/sec (corresponding to $f = 250$ Hz). In the second case, the model is suddenly loaded at a load rate of 10^6 lbs/sec to a load f_0 which is then held constant for all time.

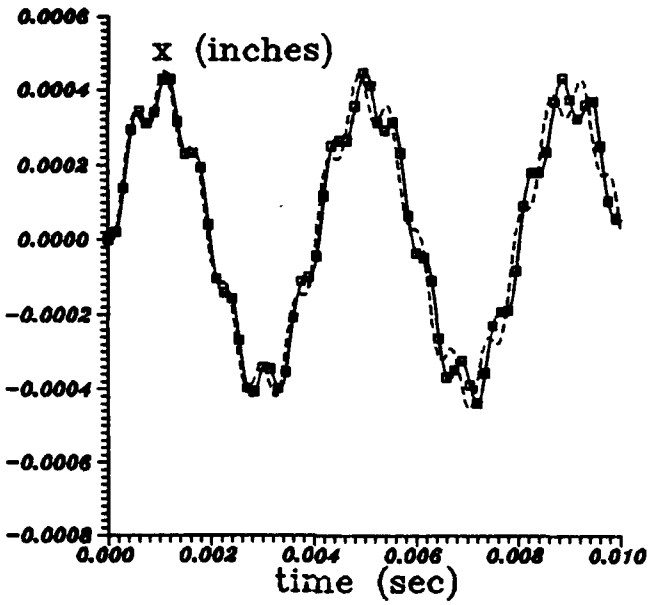

Figure 3.14. MSHELL model (solid line) vs. theory (dotted line) for $e_{rms} = 2.6\%$

The load function is therefore

$$\vec{\mathbf{f}} = \frac{1}{\sqrt{3}} \begin{bmatrix} 1 \\ 1 \\ 1 \end{bmatrix} f(t), \qquad \text{where } f(t) = \begin{cases} 10^6 t & t < f_0/10^6 \\ f_0, & t \geq f_0/10^6 \end{cases} \tag{3.4}$$

For each value of f, the minimum time step is found. The criterion for a successful run was that the maximum cumulative error, e_{rms}, never exceeded 1% over the course of the run of 0.2 seconds. The 1% value is arbitrary, but Figures 3.14 and 3.15 indicate the improvement gained in decreasing the error from 2.6% in Figure 3.14 to 1% in Figure 3.15.

For the suddenly applied load of infinite duration, there is a clear demarcation between the time step required for prebuckling and postbuckling loads. In this discussion, postbuckling implies a reversal of geometry about the supports of springs 3 and 4, i.e. the mass crosses the $w = d$ plane. Point B in Figure 3.16 represents the lowest load at which buckling occurred. The time

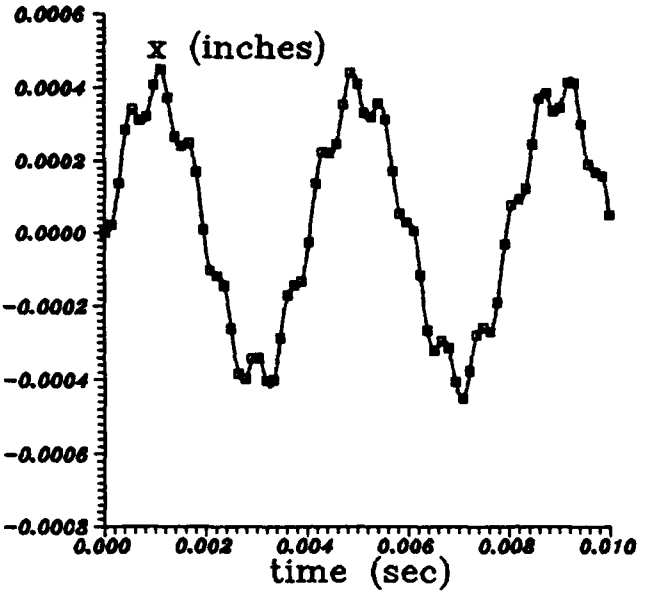

Figure 3.15. MSHELL model (solid line) vs. theory (dotted line) for $e_{rms} = 1.0\%$

step required to model postbuckling is an order of magnitude less than that required to model prebuckling. Buckling occurred at all loads beyond that of point B. The nonlinear frequency of oscillation becomes low at loads just prior to buckling, and this is the reason for the increase in Δt (point A) just prior to the buckling load.

For the sinusoidal loading case there is no clear demarcation between pre- and postbuckling loads. Over the course of the 0.2 second run, the model buckled at points E and F in Figure 3.16, but not at the two points between them. Buckling occurred at point E at $t = 0.15$ seconds, and at F at $t = 0.042$ seconds. By increasing the duration of the run, it was found that at point D (the load *prior* to point E), buckling occurred at $t = 0.487$ seconds. Surprisingly, at a still lower load (point C), buckling occurred at $t = 0.236$ seconds. For the sinusoidal loading case, the buckling occurs when the load and the inertia of the shell model are close enough in phase for a long enough time to allow buckling. These conditions occur at various times, and a higher load by no means assures a shorter time to buckling.

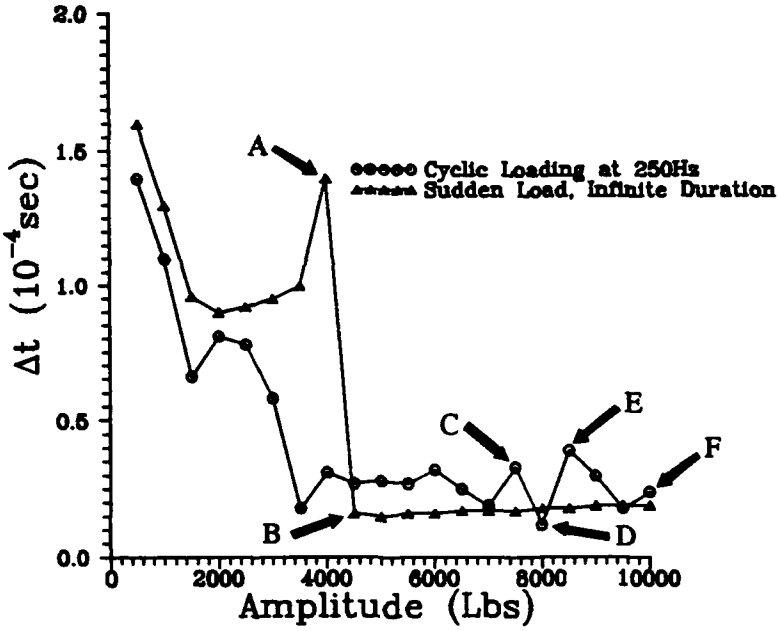

Figure 3.16. Maximum time step Δt vs. load

The highest natural frequency of the MSHELL model is f_h =618 Hz, corresponding to a period of τ_h =0.0016 seconds. For the suddenly loaded case, the suitable time step in the prebuckling case is about $\tau_h/20$, while for the postbuckling case a time step of about $\tau_h/160$ is appropriate. A time step in this region lies below the nearly horizontal line containing point B in Figure 3.16 and allows for some margin. As there is no clear demarcation in the sinusoidal loading case, the suitable time step choice is still about $\tau_h/160$.

IV. THE COMPOSITE SHELL

4.1 The Composite

A 24-ply simply supported composite cylindrical is the subject of the present research. The ply lay-up is $[0_6/90_6]_s$ and the material properties correspond to those of Hercules' AS4-3501-6 graphite epoxy composite. The material properties used are listed in Table 4.1. Because perfect

E_1	E_2	G_{12}	G_{13}	G_{23}	ν_{12}
$18.844(10^6)$	$1.468(10^6)$	$0.91(10^6)$	$0.91(10^6)$	$0.45(10^6)$	0.26

Table 4.1. Physical properties of AS4-3501-6 graphite epoxy composite

interply bonding is assumed, the composite is modeled as a 4-ply $[0/90]_s$ lay-up for the purposes of input to the finite element code. The geometry and loading of the simply supported shell are depicted in Figure 4.1. The first three natural frequencies are found from linear eigenvalue analysis and are shown in Table 4.2. The edges are simply supported along their longitudinal lengths, and

	1	2	3
$\omega(\text{sec}^{-1})$	3172	4758	9503
$f(\text{Hz})$	505	757	1512
$\tau(\text{sec})$	0.0020	0.0013	0.0007

Table 4.2. First three natural frequencies of AS4-3501-6 graphite epoxy composite shell

the sudden load is applied at Node 1. The static collapse load of the shell is 2800 lbs, and was calculated using the method of Riks (23). The shell is modeled using bilateral symmetry, which is adequate for cross-ply laminates (25:3-4). Node 107 is pointed out because it is the node furthest from DOF restraints due to either boundaries or planes of symmetry and is useful in the analysis.

4.2 Convergence

Except for the first prebuckled case study, the mesh used in the current research is the mesh formulated by Taylor (28:3-25). Silva (25:3-3) performed extensive convergence analyses and

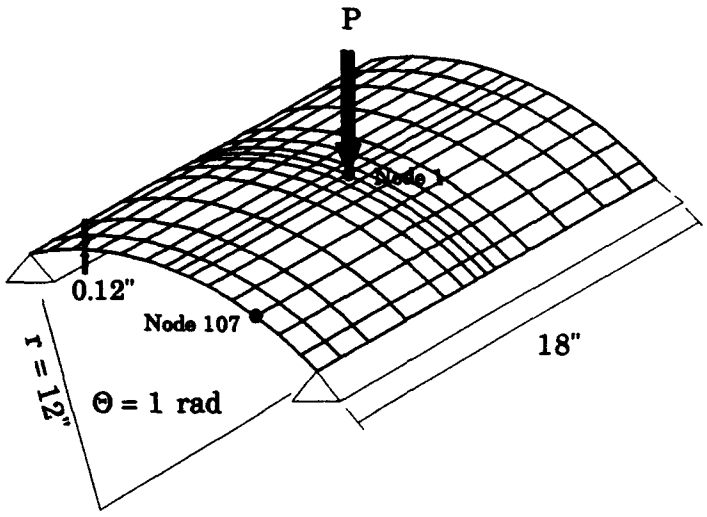

Figure 4.1. Shell geometry, boundary conditions, and loading (Taylor's mesh)

developed criteria for guaranteeing convergence (see Figure 4.2 for Silva's mesh). Taylor's mesh is used because it falls within five percent of Silva's criteria based on peak load, and the use of Taylor's mesh very significantly decreases the computer run time. His mesh is shown in Figure 4.3.

4.3 Laminate Failure

In the present research, it is assumed ply failure and delamination do not occur. An analysis by Silva (25:4-32) using the two-dimensional Tsai-Wu failure criterion showed that ply failure begins very early with the initial dimpling of the shell, and become extensive when rotations exceed 2.5 degrees. He notes, however, that laminated panels have been observed to withstand much larger rotations than these without failure. In the model used in the present research, energy applied to the shell in the form of the external load can go into elastic strain (potential) energy of the shell or

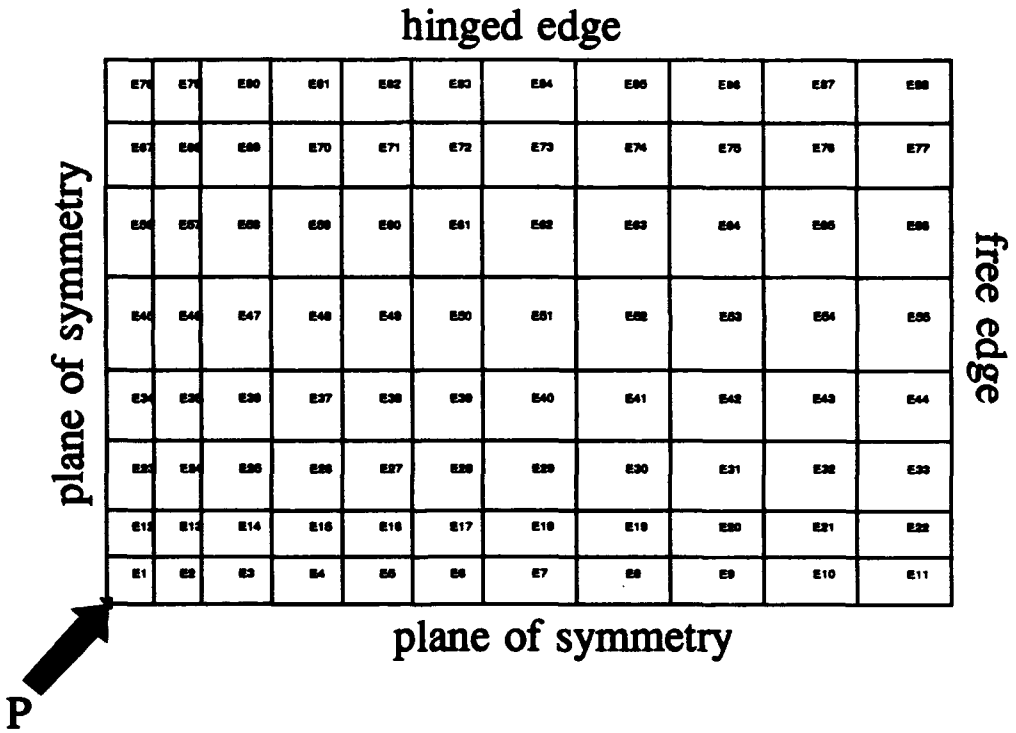

Figure 4.2. Silva's mesh

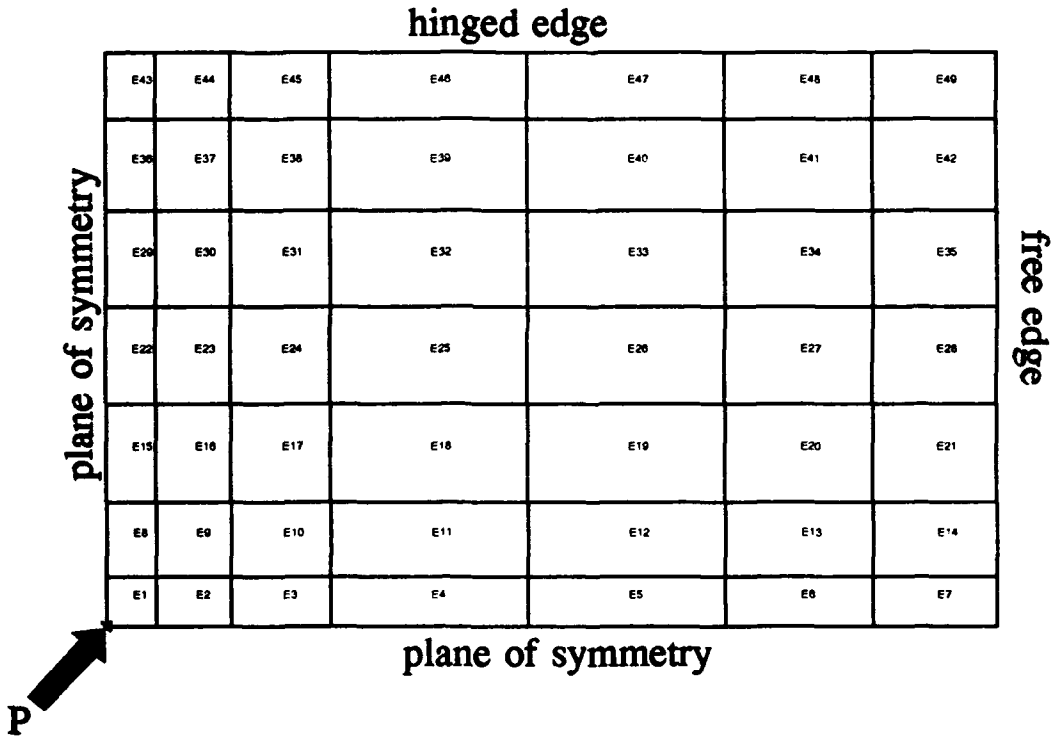

Figure 4.3. Taylor's mesh

shell movement (kinetic energy) alone. Real panels have additional thermal and plastic mechanisms to dissipate energy. This is by no means to imply that the snapping shell would not fail, but that classical failure criteria applied to these panel predict early failure. In any case, in order to study the dynamic snapping phenomena of this (and other) research, the ply failure is ignored.

4.4 Prebuckled Behavior

Prebuckled cases are those in which the suddenly applied load does not produce collapse (buckling). The result of the load is an oscillation of the shell structure.

4.4.1 The Time Step. For prebuckled motion of the shell under sudden loading, the linear eigenvalue analysis may be used to formulate the appropriate time step. The time step may be chosen based upon the first linear natural frequency, f_1 :

$$\begin{aligned} \tau_1 &= 1/f_1 \\ \Delta t &= \tau_1/20 \end{aligned} \tag{4.1}$$

This time step was found to be sufficient for all cases of prebuckled motion.

4.4.2 Case Studies. In the first case, a convergence tolerance, e_{tol} of 0.2% is chosen for the equation solver, and a time step of 0.0001 seconds is used. The load of 2000 pounds is applied at a rate of 10^6 lbs/sec. Silva's mesh (25), which has 88 elements (vs. Taylor's 49) is used. The displacement field of the shell structure becomes erratic after only three cycles (see Figure 4.1). Initially, the displacement oscillates about the node's static solution of approximately $w = 0.85$ inches, but then the displacements become large and erratic. Furthermore, these large erratic displacements appear in coordinate directions other than that of the applied load direction, w. In fact, they occur in every degree of freedom, as can be seen in the plots of displacements at the free

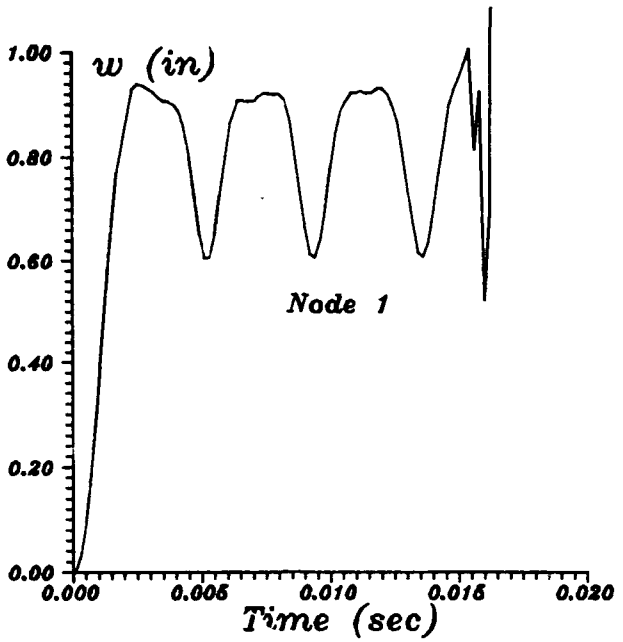

Figure 4.4. Displacement of Node 1, the point of applied load, $e_{tol} = 0.2\%$, Silva's mesh

edge node, Node 163[1] (see Figure 4.5 and Figure 4.6). The various degrees of freedom appear to exhibit instability approximately coincidentally in time (at a particular node). Because the free circumferential edge of the shell is subject to the least constraint, and because this is the region in which the in-plane displacements are largest, node number 163[2], an element-corner node on the free edge, is chosen for illustrative purposes.

Observing the motion of a nodal DOF in phase space (nodal velocity vs. displacement) is often useful. Consider the w displacement of Node 1. Figure 4.7 illustrates the nearly elliptical trajectory of this node. This is the center node of the model, and because symmetry has been invoked, all DOF at this node have been constrained except w. The very regular trajectory is hence a by-product of shell symmetry. In contrast, consider the seven-DOF node 163. The u, v, and w displacements may be seen in Figure 4.5, and the rotational displacements are depicted in

[1]Node 163 in Silva's mesh is very near Node 107 in Taylor's mesh.
[2]Near Node 107 in Taylor's mesh

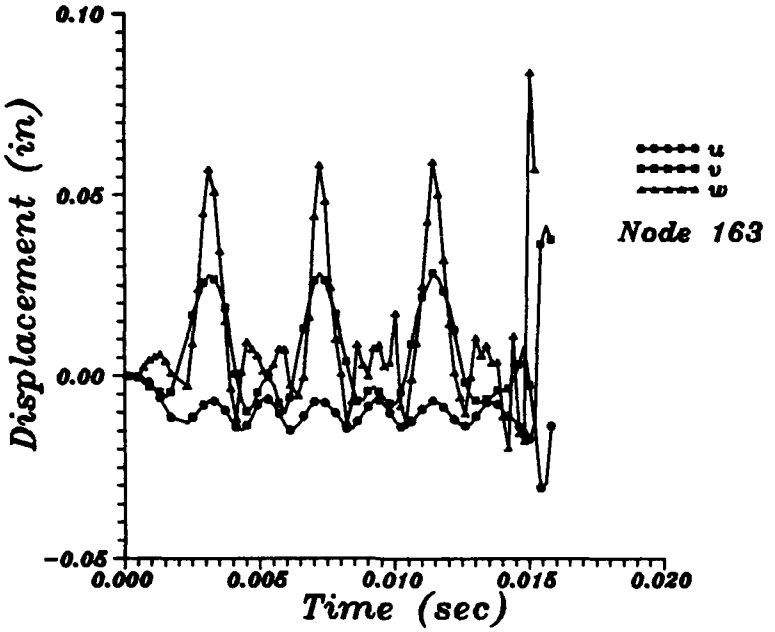

Figure 4.5. Displacement DOF vs. time at Node 163, a free edge node, $e_{tol} = 0.2\%$, Silva's mesh

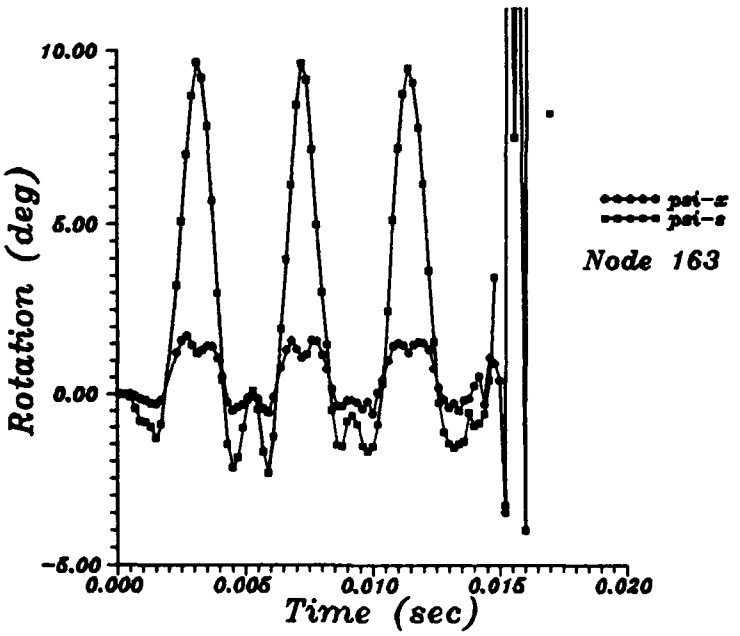

Figure 4.6. Rotational DOF vs. time, Node 163, $e_{tol} = 0.2\%$, Silva's mesh

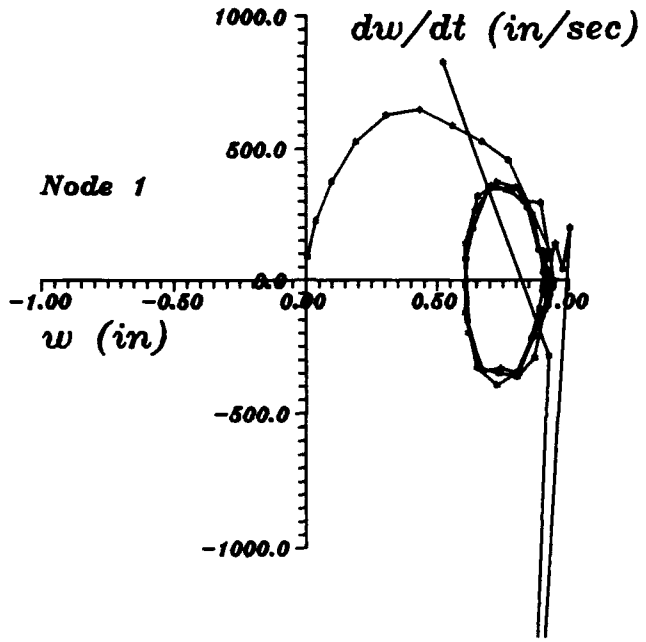

Figure 4.7. Phase space of w displacement, oscillating region, node 1, $e_{tol} = 0.2\%$, Silva's mesh, Note departure of the trajectory from phase orbit due to numerical instability

Figure 4.6. In phase space, the w trajectory in the oscillating region for node 163 (see Figure 4.8) is much less regular than that of node 1. The trajectory has two fairly distinct regions. The roughly circular regions of the trajectory correspond to the high peaks in Figure 4.5, while the collection of points near the origin correspond to the more irregular regions between those peaks. The unbounded departure of the trajectory in phase space indicates numerical instability, as the nodal velocities reach clearly unrealistic values.

Figures 4.9 and 4.10 depict the deformed shell geometries prior to and after the onset of instability. The deformed geometry associated with instability (Figure 4.10), while satisfying compatibility and potential energy constraints, is physically unreasonable. Some adjacent nodes have collapsed upon each other to form odd vertical lines and many elements are severely misshapen. Examining the deformed geometry hence provides one means of differentiating between dynamic and numerical instability.

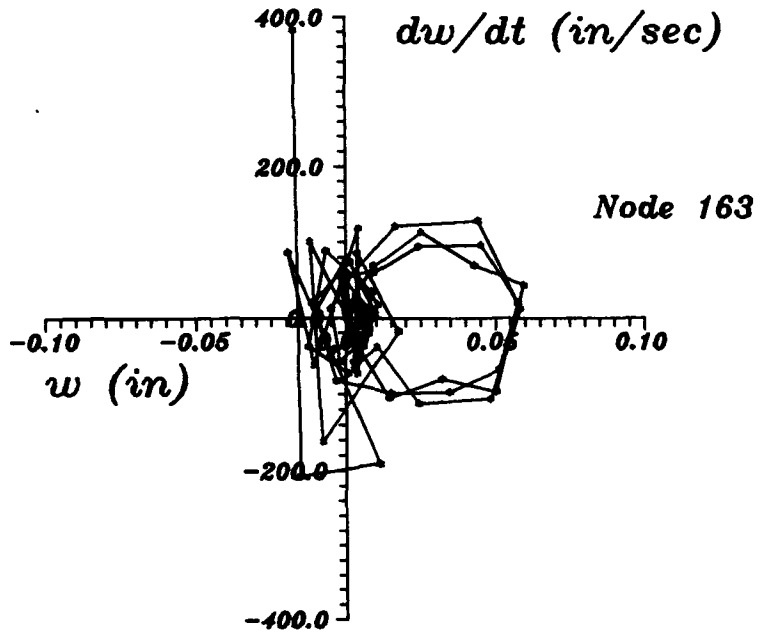

Figure 4.8. Phase space of w displacement, oscillating region, node 163, $e_{tol} = 0.2\%$, Silva's mesh

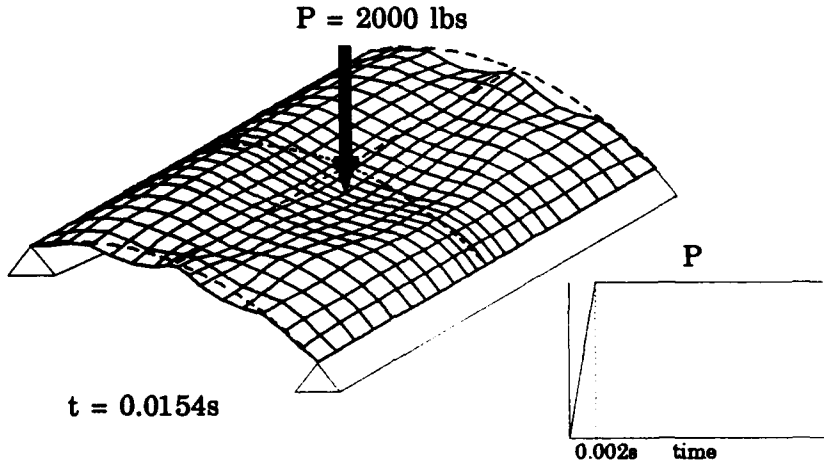

Figure 4.9. Deformed shell geometry, numerically stable region, $e_{tol} = 0.2\%$, Silva's mesh

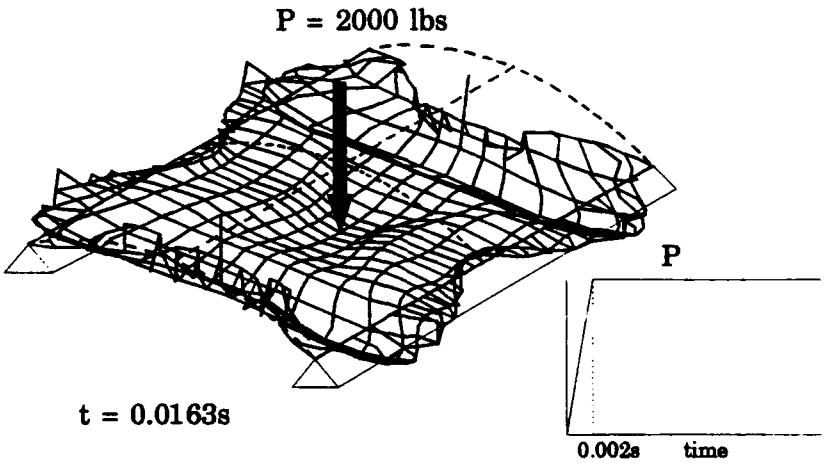

Figure 4.10. Deformed shell geometry, numerically unstable region, $e_{tol} = 0.2\%$, Silva's mesh

In the second case, two changes are made. First, a coarser mesh (Taylor's) is used and, second, the convergence tolerance for the Newton-Raphson method is reduced by a factor of 2000 to 0.0001%. Both of these changes should have the effect of improving numerical accuracy. Reducing the number of elements reduces the number of nodes by nearly a half, hence reducing the number of members in the matrices by three-quarters. The time step is unchanged. The results indicate that the onset of instability has been delayed, as no instability is observed over the length of the run.

Figure 4.11 depicts the steady-state oscillation of Node 1. At no time during the run does the displacement diverge as it did in the previous case. The use of the tighter tolerance and smaller time step has delayed the onset on instability beyond 0.03 seconds. Had the calculations been continued in time, an instability like that of the first case would likely have been seen. In fact, another run (not included here) modelling an isotropic shell did display numerical instability just

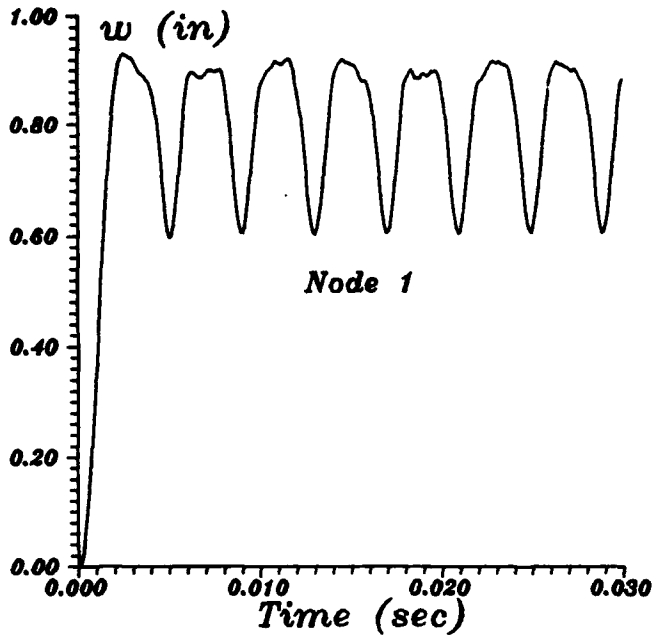

Figure 4.11. Displacement of Node 1, $e_{tol} = 0.0001\%$, Taylor's mesh

one time step prior to the end of the 0.03 second run. The phase diagram associated with activity at Node 1 is shown in Figure 4.12. Figure 4.13 shows the fundamental nonlinear frequency to be 241 Hz. This nonlinear frequency is roughly half that of the fundamental linear frequency of vibration. Figure 4.14 shows that while the displacement versus time at the shell edge is periodic and regular, the function appears to be getting noisier (i.e. more high frequency content) with time. It is not clear whether this trend is due to parametric resonance or the onset of a numerical instability. The trend is even more apparent in the velocity versus time (see Figure 4.15).

The in-plane motion of the shell is substantial even in this pre-collapse case — the circumferential (v) displacements are about one-third of the transverse (w) displacements, and the w displacements are about eight times the shell thickness. In this truly nonlinear problem, the assumption of in-plane inextensibility, common in linear shell analysis, would be grossly inadequate. The phase diagram associated with activity at Node 107 is shown in Figure 4.16.

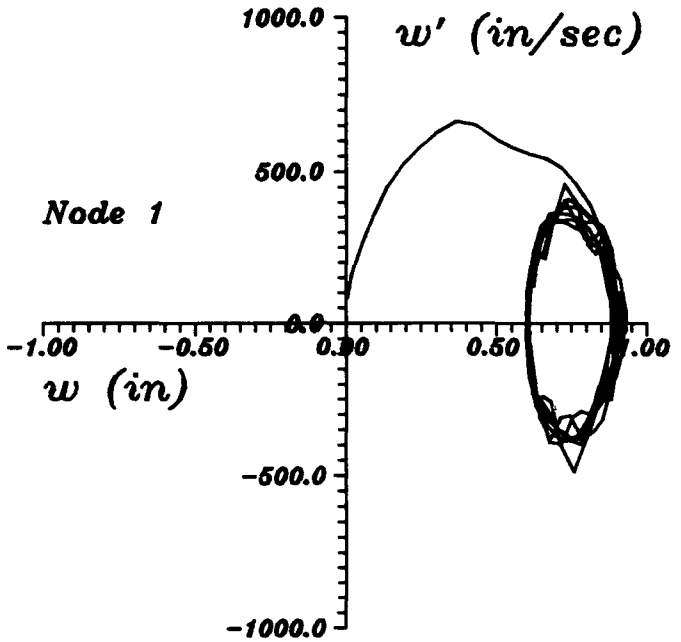

Figure 4.12. Phase trajectory of Node 1, $e_{tol} = 0.0001\%$, Taylor's mesh

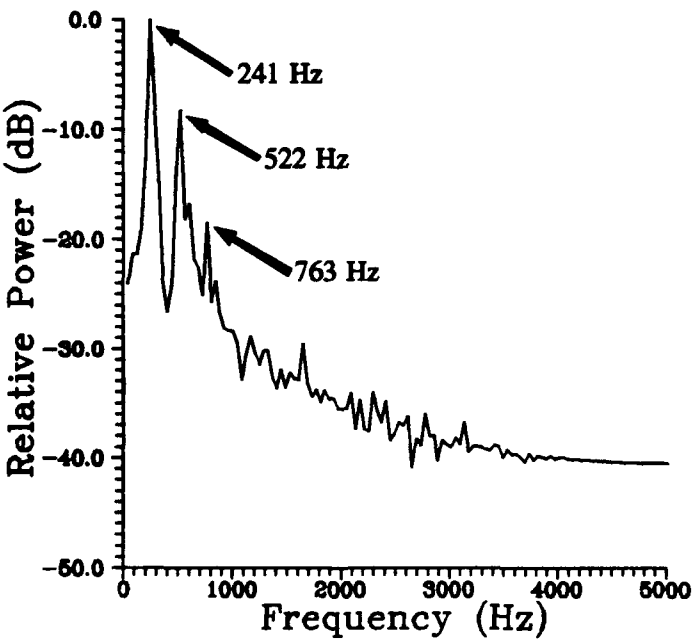

Figure 4.13. Frequency response of Node 1, $e_{tol} = 0.0001\%$, Taylor's mesh

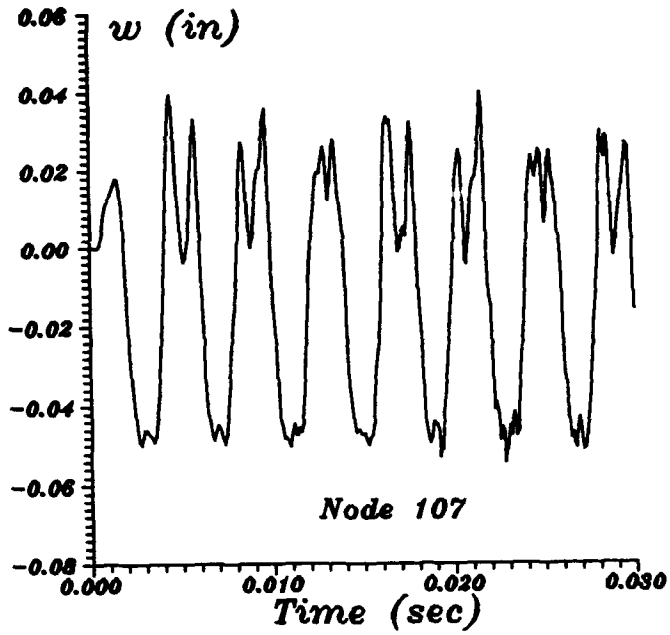

Figure 4.14. Displacement of Node 107, $e_{tol} = 0.0001\%$, Taylor's mesh

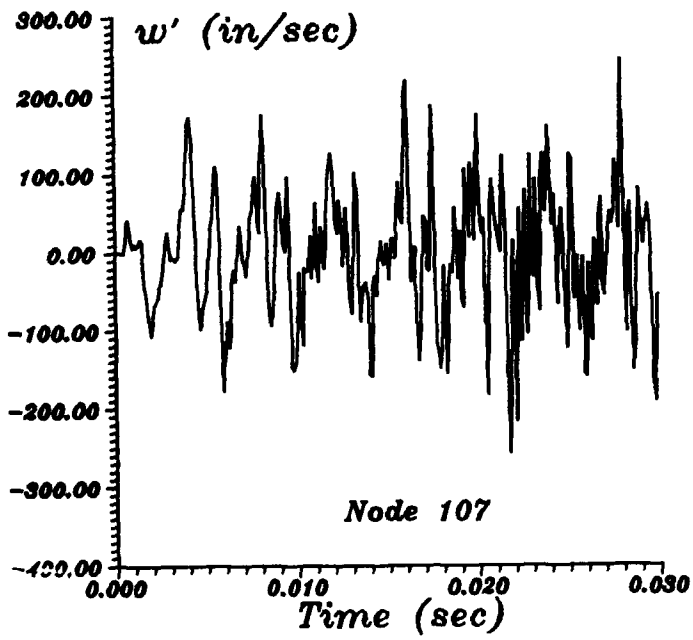

Figure 4.15. Velocity of Node 107, $e_{tol} = 0.0001\%$, Taylor's mesh

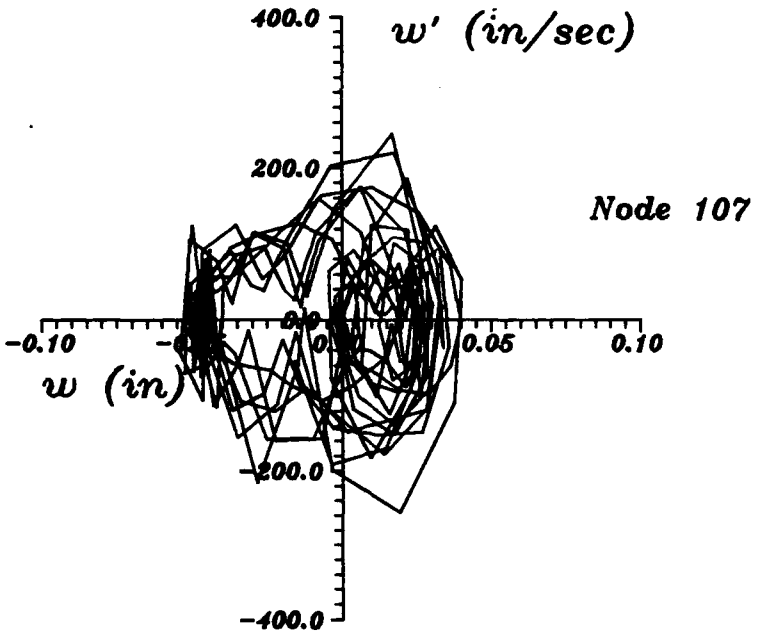

Figure 4.16. Phase trajectory of Node 107, $e_{tol} = 0.0001\%$, Taylor's mesh

The frequency response at the shell edge, shown in Figure 4.17, is much more complex than that of Node 1. The response in general is broad-banded and may imply a near-chaotic condition or imminent numerical instability. The frequency response in the u (longitudinal in-plane) direction of the entire quarter panel of the shell may be seen in Figures 4.18 and 4.19. These figures represent the relative power spectrum, $S(\omega)$, for the fundamental nonlinear frequency of about 242 Hz and the third harmonic (near 763 Hz) respectively. In the figures, $S(\omega)$ is depicted relative to the maximum $S(\omega)$ of the fundamental frequency. It is interesting to note that the maximum values of $S(\omega)$ in Figure 4.19 do not lie at the free edge of the shell, but rather along the $s = 0$ axis of symmetry. Similarly, the maximum values of $S(\omega)$ in the v direction take place along the $x = 0$ axis of symmetry.

As a final case, an isotropic shell of the same physical dimensions was analyzed. The elastic modulus of the shell was adjusted to match the static collapse strength of the composite so that

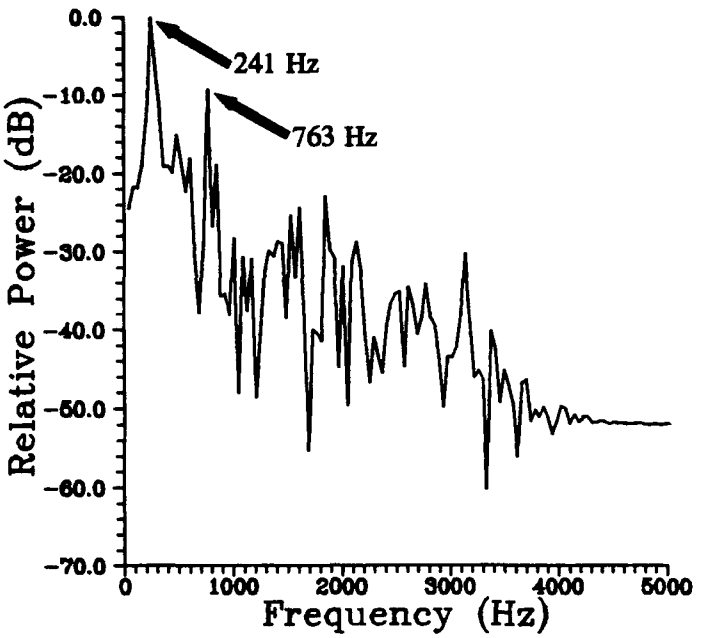

Figure 4.17. Frequency response of Node 107, $e_{tol} = 0.0001\%$, Taylor's mesh

the effects of anisotropy could be emphasized. The behavior of the isotropic shell was very similar to that of its composite counterpart. However, the isotropic shell was slightly more flexible than the composite. The maximum displacements were about 5, 17, and 6 percent greater in the u, v, and w directions, respectively, for the isotropic shell.

4.5 Postbuckled Behavior

Postbuckled behavior refers to cases involving the phenomenon of dynamic buckling or snap-through and, in this context, is the result of a suddenly applied load of infinite duration.

The methodology for choosing the appropriate time step(s) is an integral part of the case studies that follow, so they are presented together.

In Taylor's work with dynamic cross-ply shells, the smallest time step used was $\Delta t = 0.0001$ seconds (18:1652). This time step failed to capture the postbuckling behavior of the shell (28:3-30).

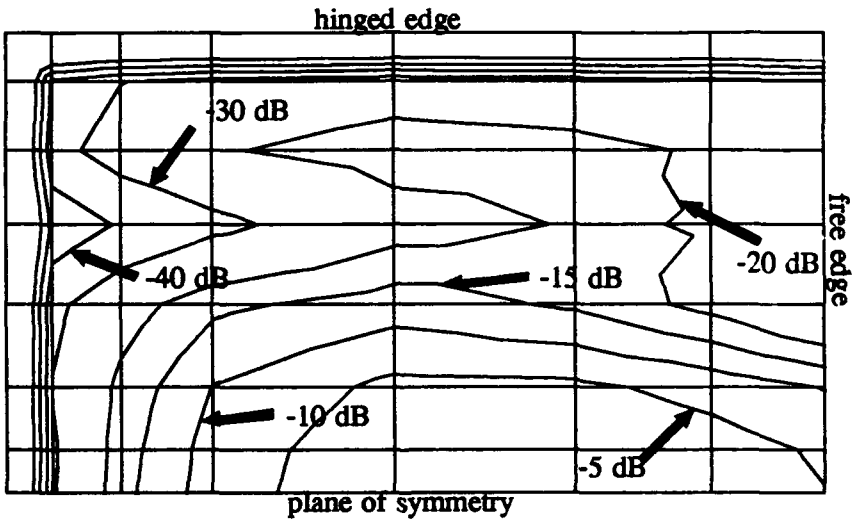

Figure 4.18. Power Spectrum $S(\omega)$ near fundamental nonlinear frequency of oscillation, $f = 242$ Hz, for u displacements

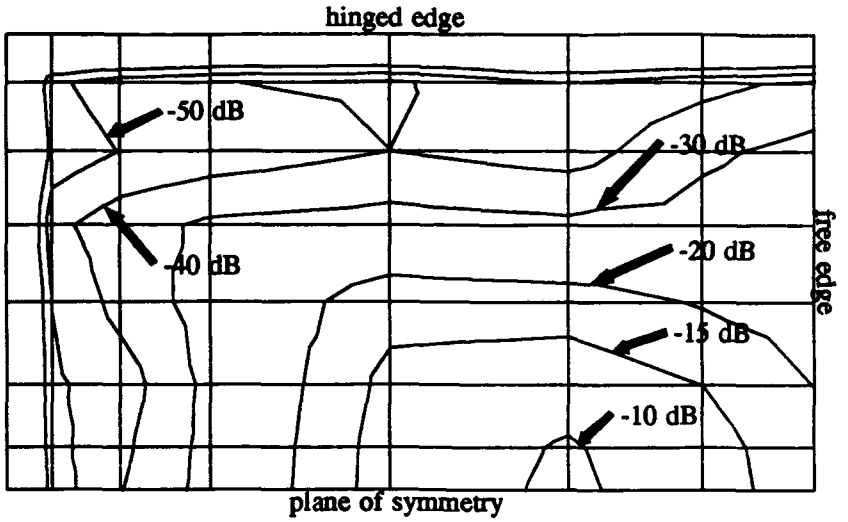

Figure 4.19. Power Spectrum $S(\omega)$ near third harmonic of fundamental nonlinear frequency of oscillation, $f = 763$ Hz, for u displacements

As a first attempt, a uniform time step half that of Taylor's ($\Delta t = 0.00005$ seconds) is used in evaluating the dynamic snapping of the cross-ply shell. The w displacement vs. time is seen in Figure 4.20. Prior to collapse, the highest frequency of interest is not associated with the shell, but with the suddenly applied load. If the ramping up of the load is considered to be the first quarter of a sinusoid, the 'frequency' of the applied load is about 125 Hz. The time step of 0.00005 seconds corresponds to a frequency of 20,000 Hz and is certainly smaller than necessary to capture the behavior in the prebuckled regime. However, the time step does not appear small enough to capture the behavior after buckling. Figure 4.21 indicates the number of iterations required to converge at each time step. The Newton-Raphson iteration requires an inordinant number of iterations to converge in the postbuckling regime (beginning near step 85), at one point requiring nearly 100 steps to converge. An examination of the Node 1 velocity data indicates that the run begins to produce unrealistic results in the neighborhood of step number 125, as the nodal velocities

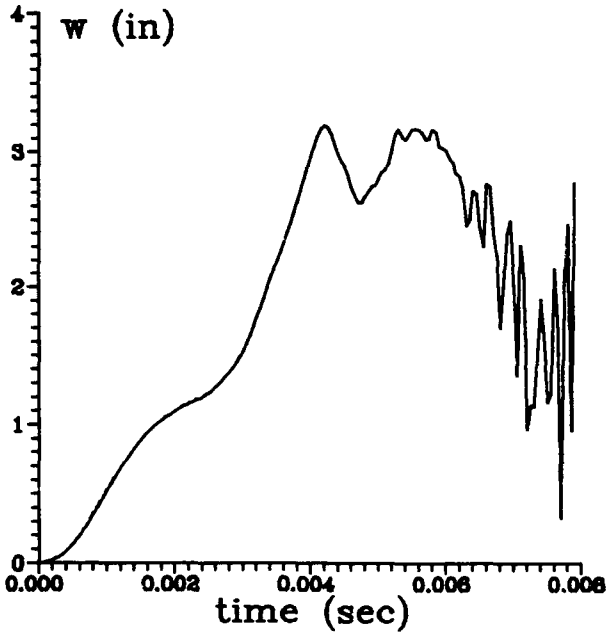

Figure 4.20. Displacement vs. time for fixed $\Delta t = 0.00005$ seconds, Taylor's mesh

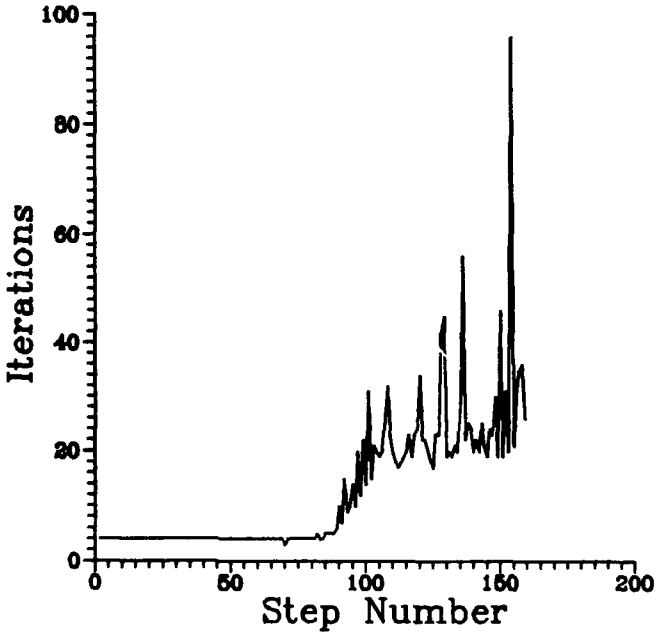

Figure 4.21. Number of iterations required vs. time step for fixed $\Delta t = 0.00005$ seconds

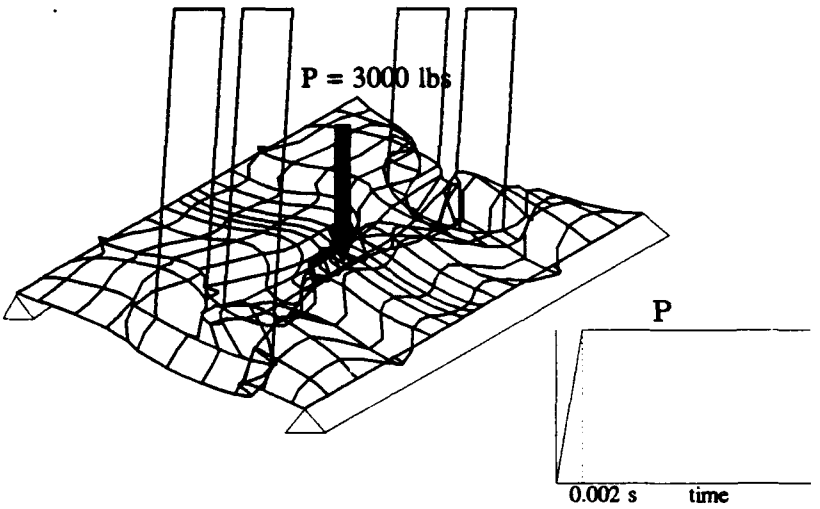

Figure 4.22. Deformed geometry of postbuckled shell indicating numerical instability, Δt = 0.00005 seconds, Taylor's mesh,

become extreme. It is noteworthy that a cursory examination of the nodal displacement versus time (Figure 4.20) does not give an indication as to the validity of the data. Once again, the deformed geometry (Figure 4.22) gives an immediate indication that something has gone numerically wrong. Figure 4.23 indicates a deformed geometry in postbuckling that does not suffer from numerical instability.

The postbuckled behavior of the composite cross-ply shell was then analyzed using Taylor's mesh and the adaptive time step method described in section 3.4 on page 3-11 with otherwise identical run parameters. A time step based upon the lowest linear frequency, f_1, (from the eigenvalue analysis) was used during that portion of the run describing initial collapse of the shell. The high-frequency content is negligible until Node 1 reaches its maximum w deflection, i.e., the shell 'bottoms out'. Shortly after this point (in this run, at t = 0.0049 sec) parametric (in-plane) resonances cause the higher frequencies to become important. Hence, a postbuckling (collapsed)

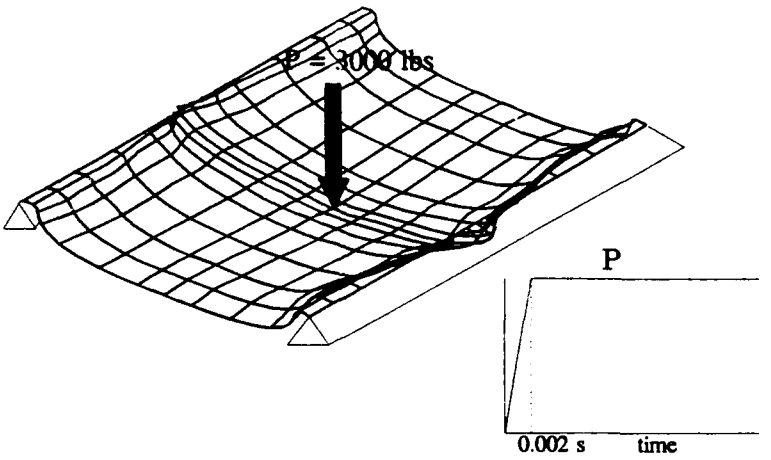

Figure 4.23. Deformed geometry of postbuckled shell, adaptive time step, Taylor's mesh

time step based upon the highest frequency of interest seen in the oscillating shell, $f_h = 760$ Hz, is used thereafter (see Figure 4.17 on page 4-15). The highest frequency of interest was arbitrarily chosen as the highest frequency within 10 dB of the maximum (from data at the most flexible portion of the structure, i.e. Node 107).

Using these frequencies with the criteria developed using the MSHELL simplified model, we have

$$\begin{aligned} \tau_{pre} &= 1/f_1 \approx 0.002\text{sec} \\ \Delta t_{pre} &= \tau_{pre}/20 \approx 0.0001\text{sec} \end{aligned} \tag{4.2}$$

$$\begin{aligned} \tau_{post} &= 1/f_h \approx 0.00131\text{seconds} \\ \Delta t_{post} &= \tau_{post}/160 \approx 8(10^{-6})\text{seconds} \end{aligned} \tag{4.3}$$

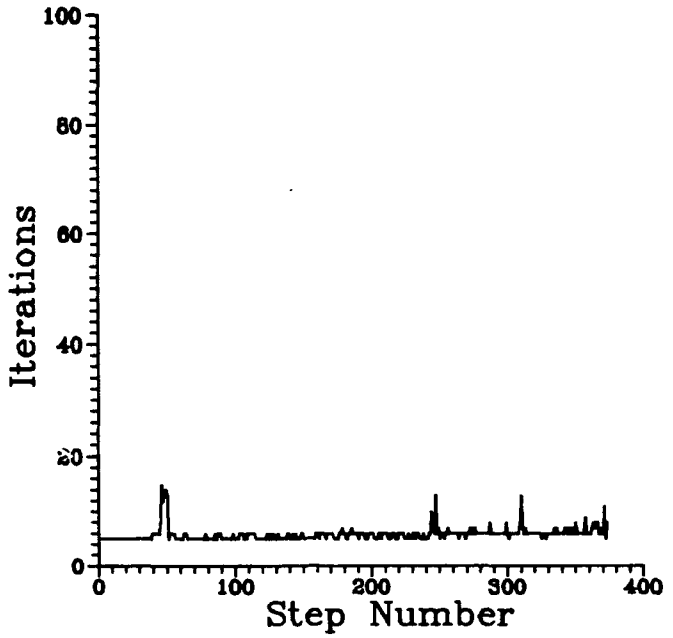

Figure 4.24. Number of iterations required vs. time step for adaptive Δt

Table 4.3 indicates the result of using the adaptive technique. In the table, I_{tot} is the total number

Method	I_{tot}	$\bar{I}$	CPU seconds
$\Delta t = 0.00005$ (fixed)	1698	11.3	20,000
Adaptive Δt	2208	5.9	31,250
$\Delta t = \Delta t_{post}$ (est.)	5500	6	80,000

Table 4.3. Comparison of time step schemes for buckling of composite cross-ply shell

of iterations performed over the run, $\bar{I}$ is the average number of iterations per time step, and *CPU seconds* refers to CPU seconds of run time on the CRAY X-MP/216. As previously mentioned, the time step of 0.00005 seconds failed to adequately model the collapsing shell throughout the run. However, Table 4.3 shows that using Δt_{post} as the time step for the entire run is not a good option. The adaptive time step technique offers substantial improvement. Figure 4.24 indicates how the number of iterations per time step was maintained at a reasonable level throughout the run.

As in other schemes for nonlinear analysis, *a priori* knowledge of the system's characteristics

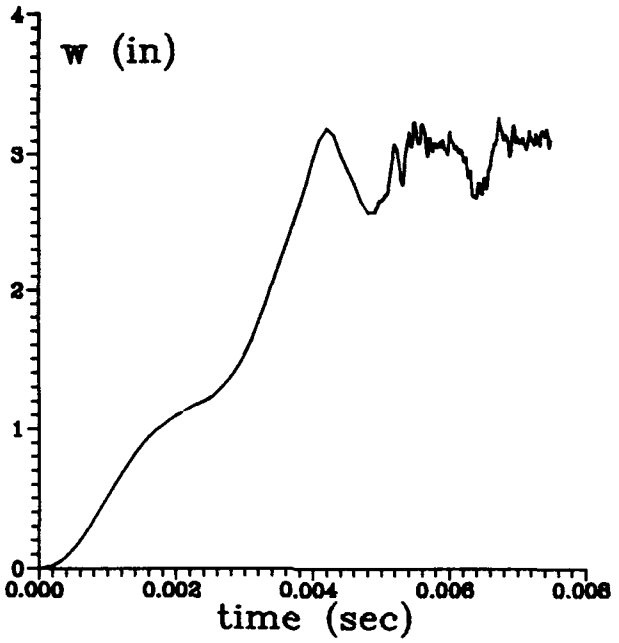

Figure 4.25. Displacement vs. time of Node 1. adaptive Δt, Taylor's mesh, collapse case

is required. However, a FFT analysis of a few cycles of the steady state oscillating behavior may provide enough data to proceed with minimum trial and error. The time step for this trial run may be chosen based on the linear eigenvalue analysis as in Section 4.4 on page 4-5.

Figure 4.25 describes the w displacement Node 1, and Figure 4.26 is the phase portrait of the motion (for the postbuckled region only). The frequency response in the postbuckled regime is shown in Figure 4.27. It displays quantitatively the same sort of broad-banded noise associated with the chaotic motion of the MSHELL simplified model (see Figure 3.11 on page 3-10).

4.6 Propagation of Displacements

The nodes in Figure 4.28 were chosen to attempt to observe the path of propagation of displacements, as they lie approximately along a line from Node 107 to the panel center. Figure 4.29 indicates how the amplitude of the rebound after buckling increases moving outward from the panel

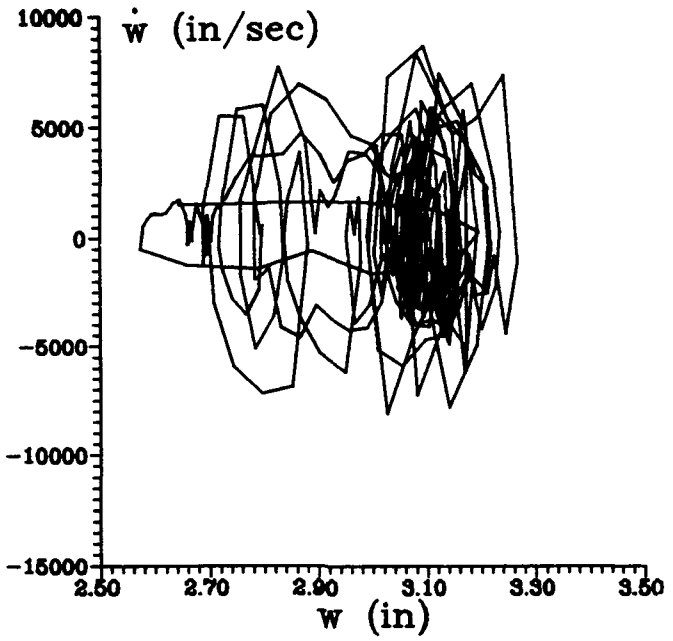

Figure 4.26. Phase diagram of Node 1, Taylor's mesh, collapsed regime only

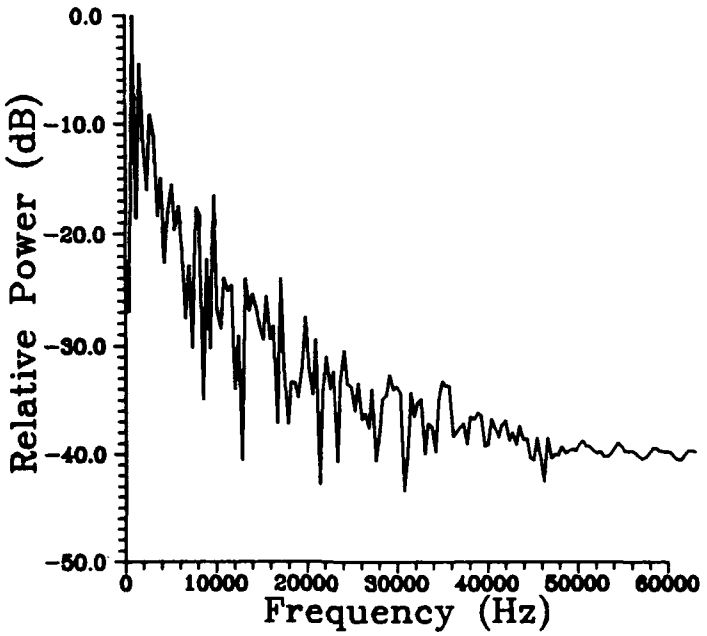

Figure 4.27. Frequency response, post buckling, adaptive time step

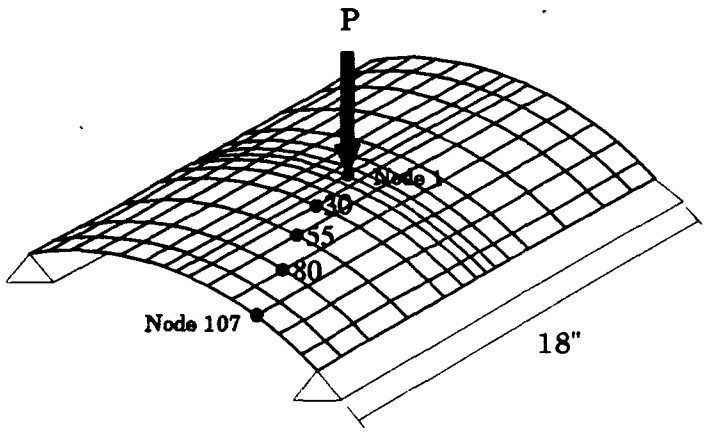

Figure 4.28. Shell geometry indicating nodes used for propagation study

center and is greatest at the free edge. The three-dimensional view of Figure 4.30 also indicates how the displacement at the edge lags the center, but the rebound amplitude is larger. The frequency responses of these nodes is shown in Figure 4.31. All nodes display the broadband frequency response associated with chaos, with the roll-off (decrease in the power spectrum with increase in frequency) being faster further from the panel center.

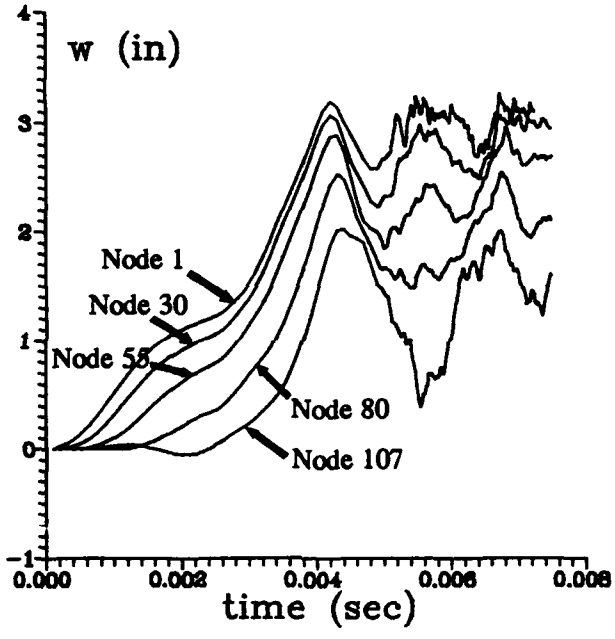

Figure 4.29. Displacement vs. time for nodes lying on a line from panel edge to panel center

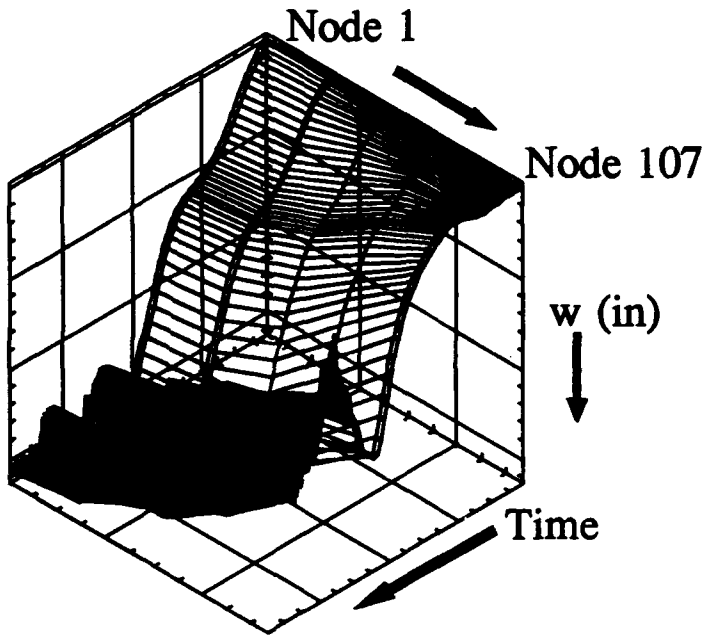

Figure 4.30. Three dimensional view of displacement of nodal line vs. time

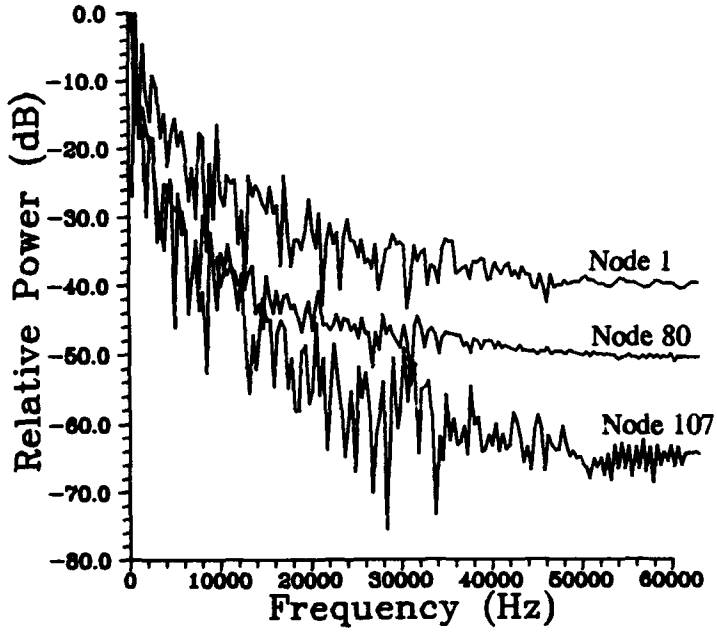

Figure 4.31. Frequency response of nodes lying along a line from panel center to panel edge, postbuckling, Taylor's mesh

V. SUMMARY, CONCLUSIONS, AND RECOMMENDATIONS

5.1 Summary

The finite element model used in this research (DSHELL) incorporates many nonlinear features that defy closed form solution. The interaction of the hundreds of displacement and rotational degrees-of-freedom complicate analysis of the problem. At the present time, only a numerical (computer) solution is available for solving the matrices of nonlinear equations involved. Hence, the numerical parameters take on major importance. Changes in the time step, (Δt), have a dramatic effect on the problem solution. Time steps that are too large cause the unconditionally stable (*not* unconditionally *accurate*) integration scheme to converge to an incorrect result for the nodal displacements and rotations. This, in turn, results in erratic and unrealistic deformed geometries of the structure.

In an attempt to study the features of this complex problem on a smaller scale, a simple shell model (MSHELL) was developed capturing many of the features of the DSHELL finite element model. The model properties were adjusted to match the geometry, static collapse load, and first linear natural frequency of the finite element model. Through sinusoidal excitation of the model, the mass in MSHELL exhibits behavior in many respects similar to that of a single node in the mesh (excepting rotational behavior). MSHELL was also used to examine the sensitivity of the accuracy in the numerical integration scheme to Δt.

Much of the nodal displacement data were taken from DSHELL runs and transformed through the Fast Fourier Transform (FFT) to the frequency domain. The FFT data were used to investigate amplitudes of the vibrations of the shell at various frequencies. An attempt was made to find trends in the propagations of nodal displacements as the shell vibrated, and a comparison was made between the the composite shell and an isotropic shell of the same physical dimensions and static collapse strength.

5.2 Conclusions

5.2.1 The Time Step The choice of time step for the finite element model is both important and difficult. For the prebuckling analysis, computation of a suitable time step is straightforward and comes from the linear eigenvalue analysis. For runs involving collapse, an adaptive time step method, in which the time step is varied over the course of the run in accordance with the criteria derived from the MSHELL simplified model, can make the run more computationally efficient. The method only applies to cases in which the loading frequency (in terms of load rate, for the sudden load of infinite duration case) is less than the highest frequency of interest in the nonlinear oscillation of the shell. Where this is not true, the time step must be chosen based upon the excitation frequency.

5.2.2 Chaos

5.2.2.1 Prebuckled Case. In the prebuckled cases examined, chaoslike behavior was not seen either in the MSHELL model or the DSHELL finite element model. Fourier analyses show that despite the relatively erratic behavior in the time domain, the motion is a combination of oscillations at discrete frequencies associated with the nonlinear oscillation of the system. Frequency analysis at the free edge node did indicate a general broadening of the response indicating near-chaotic behavior or possibly nearing the onset of numerical instability. In-plane displacements were found to be significant — on the order of one-third the transverse displacements. This parametric resonance is clearly captured by DSHELL.

Comparisons between the composite and isotropic shell indicated very similar behavior, except that the maximum displacements in the isotropic shell (of the same physical dimensions and static collapse strength as the composite shell) were larger, especially in the circumferential direction.

5.2.2.2 Postbuckled Case. Chaoslike behavior was observed in both the MSHELL model and the DSHELL finite element model. The broad banded frequency spectra of the oscil-

lations and the very irregular, but bounded, trajectories in phase space are consistent with chaos. Analysis with the MSHELL model shows that the dynamic buckling load is not a meaningful parameter in the presence of cyclic loading. Buckling occurs under specific conditions not directly proportional to the amplitude of the forcing function.

5.2.3 Numerical Instability The DSHELL finite element code has a threshold for numerical instability that is likely a function of the following parameters.

- the number of unrestrained DOF (mesh size)
- the convergence tolerance of the Newton-Raphson scheme
- the total number of iterations performed over the length of the run (a function of the time step and, to a lesser extent, the convergence tolerance)

Cases with large numbers of DOF (fine meshes), large convergence tolerances, and large time steps will suffer numerical instability in the shortest time. Because fine convergence tolerances do not significantly increase the number of iterations per time step, a small tolerance ($e_{tol} \leq 10^{-6}$) should routinely be used. A time step that is too small increases the number of calculations unnecessarily and hastens the onset of numerical instability. The adaptive time step method presented herein can use computer time more efficiently.

The deformed geometry plots give an immediate, though qualitative, indication of numerical instability while observation of the displacement of a single DOF versus time may not. In cases of numerical instability, DSHELL is usually able to converge to a solution that satisfies compatibility and potential energy constraints while arriving at an unrealistic deformed geometry. Unbounded trajectories in phase space also indicate numerical instability and give quantitative information as to the onset.

5.3 Recommendations

5.3.1 The Time Step. Unlike multi-step methods, in which changing the time step Δt is not pragmatically possible during the run (13:1346), the single-step beta-m method can easily accommodate varying Δt (13:1350). The DSHELL computer code could be modified to vary the time step in response to the rate of change of one or more variables. In this way, much computer time could be saved by lengthening Δt in those parts of the run (e.g., prebuckling or steady-state oscillation) that do not require a short time step. This would also allow longer runs to be performed with meaningful results (numerical error accumulation could be much delayed).

*5.3.2 The Beta-*m *Method.* The beta-m method allows the user to modify the stability and accuracy of the algorithm through the choice of the coefficients, β_i. For the current (and prior) research, the β_i were chosen to yield unconditional stability. Optimum choices of these coefficients may exist based upon the type of problem being investigated. Confidence gained in the choice of time step allows the investigator to shift emphasis from unconditional convergence to higher accuracy.

5.3.3 Convergence Tolerance. In the current research, the convergence tolerance used for the Newton-Raphson iteration technique was practically eliminated as a variable by choosing a minute value. Relaxation of the convergence tolerance might yield somewhat faster computer runs, though the interaction between the convergence tolerance and the time step is not fully understood. The time step has a more pronounced effect on the number of iterations required for convergence. Future research could investigate this relationship.

5.3.4 Modern Nonlinear Analysis. Modern nonlinear analysis involves a host of techniques not applied in the current research. These include study of the Lyapunov exponents, fractal dimensions, and many mor graphical techniques (logistic maps, circle maps, horseshoe maps, etc.) not presented here. While the DSHELL model would be too cumbersome for most of these methods,

the MSHELL model could be used to explore many of the phenomena associated with buckling shells.

5.3.5 Optimization of DSHELL. The DSHELL code could be optimized to choose an initial time step and convergence tolerance based on the problem presentation. The program could adjust these parameters based upon the dynamic behavior involved. For example, the program could be made to recognize the counter-flexural point associated with imminent snap-buckling and adjust the time step accordingly. Vectorization of the current DSHELL code is probably not practical, but a new vectorized code based upon the same theory could be written. This would be a major task, but the time involved in running the current code (even on the supercomputer) is formidable.

Appendix A. *Derivation of MSHELL Equations of Motion*

The simplified shell model is depicted in Figure 2.3 on page 2-9, and its appearance as it relates to the shell geometry is shown in Figure 2.4 on page 2-10. All springs are of undeformed length b, and springs 1 and 2 remain horizontal regardless of the deformed geometry (the ends of springs 1 and 2 can be thought of as riding in tracks that have no resistance to vertical motion of the spring ends). The object is of mass m, and the dimensions h and d are the projections of undeformed spring 3 (or 4) on the horizontal and vertical, respectively. Given the vector of displacements $\vec{\mathbf{x}} = [\ u \quad v \quad w\ ]^T$, the deformed spring lengths, b_i are

$$\begin{aligned} b_1 &= \left[(b-u)^2 + v^2\right]^{1/2} \\ b_2 &= \left[(b+u)^2 + v^2\right]^{1/2} \\ b_3 &= \left[(h+v)^2 + (d-w)^2 + u^2\right]^{1/2} \\ b_4 &= \left[(h-v)^2 + (d-w)^2 + u^2\right]^{1/2} \end{aligned} \tag{A.1}$$

and the change in length of each spring is given by $\Delta_i = b_i - b$:

$$\begin{aligned} \Delta_1 &= b_1 - b = \left[(b-u)^2 + v^2\right]^{1/2} - b \\ \Delta_2 &= b_2 - b = \left[(b+u)^2 + v^2\right]^{1/2} - b \\ \Delta_3 &= b_3 - b = \left[(h+v)^2 + (d-w)^2 + u^2\right]^{1/2} - b \\ \Delta_4 &= b_4 - b = \left[(h-v)^2 + (d-w)^2 + u^2\right]^{1/2} - b \end{aligned} \tag{A.2}$$

The force generated by each of the springs is

$$\vec{\mathbf{f}}_i = k_i \Delta_i \hat{\mathbf{e}}_i \tag{A.3}$$

where k_i are the linear spring stiffnesses. The direction of each of the forces is given by

$$\hat{\mathbf{e}}_i = \frac{\vec{\mathbf{V}}_i}{\|\vec{\mathbf{V}}_i\|} \tag{A.4}$$

where $\vec{\mathbf{V}}_i$ represents a vector of length b_i pointing along the spring in the direction of the force generated by a positive Δ_i . The unit vectors, $\hat{\mathbf{e}}_i$, are thus easily written component-wise as

$$\begin{aligned}
\hat{\mathbf{e}}_1 &= [(b-u)\hat{\mathbf{i}} - v\hat{\mathbf{j}} + 0\hat{\mathbf{k}}]/b_1 \\
\hat{\mathbf{e}}_2 &= [-(b+u)\hat{\mathbf{i}} - v\hat{\mathbf{j}} + 0\hat{\mathbf{k}}]/b_2 \\
\hat{\mathbf{e}}_3 &= [-u\hat{\mathbf{i}} - (h+v)\hat{\mathbf{j}} + (d-w)\hat{\mathbf{k}}]/b_3 \\
\hat{\mathbf{e}}_4 &= [-u\hat{\mathbf{i}} + (h-v)\hat{\mathbf{j}} + (d-w)\hat{\mathbf{k}}]/b_4
\end{aligned} \tag{A.5}$$

Summing the forces contributed by the deformed springs, we have

$$\vec{\mathbf{f}} = \sum_i k_i \Delta_i \hat{\mathbf{e}}_i \tag{A.6}$$

We include a very simple model of viscous damping by assuming that the velocity of the mass is resisted equally in all directions by an amount proportional to the velocity in that direction. That is

$$\vec{\mathbf{f}}_{damping} = -c\dot{\vec{\mathbf{x}}} \tag{A.7}$$

where $c > 0$ is the damping coefficient and $\dot{\vec{\mathbf{x}}}$ represents the vector of velocities $\dot{u}, \dot{v}$, and $\dot{w}$. This is a significant simplification over the DSHELL model, which utilizes a proportional damping scheme:

$$\mathbf{C} = 2\xi\omega\mathbf{M} \tag{A.8}$$

Where ξ is the damping ratio and ω is the linear fundamental natural frequency (6:727). We further allow for a forcing function that may vary with time:

$$\vec{\mathbf{f}}_{forcing} = \vec{\mathbf{f}}(t) \tag{A.9}$$

Setting these forces equal to the inertial force of the mass yields

$$\begin{aligned} m\ddot{\vec{\mathbf{x}}} &= \vec{\mathbf{f}}_{springs} + \vec{\mathbf{f}}_{damping} + \vec{\mathbf{f}}_{forcing} \\ &= k_1\Delta_1\hat{\mathbf{e}}_1 + k_2\Delta_2\hat{\mathbf{e}}_2 + k_3\Delta_3\hat{\mathbf{e}}_3 + k_4\Delta_4\hat{\mathbf{e}}_4 - c\dot{\vec{\mathbf{x}}} + \vec{\mathbf{f}}(t) \end{aligned} \tag{A.10}$$

Substituting Eqs (A.2) and (A.5) into Eq (A.10) yields

$$\begin{aligned} m\ddot{\vec{\mathbf{x}}} &= \vec{\mathbf{f}}_{springs} + \vec{\mathbf{f}}_{damping} + \vec{\mathbf{f}}_{forcing} \\ &= k_1(b_1 - b)\left[(b-u)\hat{\mathbf{i}} - v\hat{\mathbf{j}} + 0\hat{\mathbf{k}}\right]/b_1 + \\ &\quad + k_2(b_2 - b)\left[-(b+u)\hat{\mathbf{i}} - v\hat{\mathbf{j}} + 0\hat{\mathbf{k}}\right]/b_2 + \\ &\quad + k_3(b_3 - b)\left[-u\hat{\mathbf{i}} - (h+v)\hat{\mathbf{j}} + (d-w)\hat{\mathbf{k}}\right]/b_3 + \\ &\quad + k_4(b_4 - b)\left[-u\hat{\mathbf{i}} + (h-v)\hat{\mathbf{j}} + (d-w)\hat{\mathbf{k}}\right]/b_4 - \\ &\quad - c\dot{\vec{\mathbf{x}}} + \vec{\mathbf{f}}(t) \end{aligned} \tag{A.11}$$

which may be factored as

$$\begin{aligned} m\ddot{\vec{\mathbf{x}}} &= \hat{\mathbf{i}}\left[k_1(b-u) - \frac{bk_1(b-u)}{b_1} - k_3u + \frac{bk_3u}{b_3} - k_4u + \frac{bk_4u}{b_4} - k_2(b+u)\right. \\ &\quad \left. + \frac{bk_2(b+u)}{b_2} - c\dot{u} + f_u\right] \\ &\quad + \hat{\mathbf{j}}\left[k_4(h-v) - \frac{bk_4(h-v)}{b_4} - k_1v + \frac{bk_1v}{b_1} - k_2v + \frac{bk_2v}{b_2}\right. \\ &\quad \left. - k_3(h+v) + \frac{bk_3(h+v)}{b_3} - c\dot{v} + f_v\right] \end{aligned}$$

$$+\hat{\mathbf{k}}\left[k_3(d-w)-\frac{bk_3(d-w)}{b_3}+k_4(d-w)-\frac{bk_4(d-w)}{b_4}\right.$$
$$\left.-c\dot{w}+f_w\right] \tag{A.12}$$

Gathering by vector component yields

$$\begin{aligned}
\hat{\mathbf{i}}: \quad m\ddot{u} = \; & k_1(b-u)-\frac{bk_1(b-u)}{b_1}-k_3u+\frac{bk_3u}{b_3}-k_4u+\frac{bk_4u}{b_4} \\
& -k_2(b+u)+\frac{bk_2(b+u)}{b_2}-c\dot{u}+f_u \\
\hat{\mathbf{j}}: \quad m\ddot{v} = \; & k_4(h-v)-\frac{bk_4(h-v)}{b_4}-k_1v+\frac{bk_1v}{b_1}-k_2v+\frac{bk_2v}{b_2} \\
& -k_3(h+v)+\frac{bk_3(h+v)}{b_3}-c\dot{v}+f_v \\
\hat{\mathbf{k}}: \quad m\ddot{w} = \; & k_3(d-w)-\frac{bk_3(d-w)}{b_3}+k_4(d-w)-\frac{bk_4(d-w)}{b_4} \\
& -c\dot{w}+f_w
\end{aligned} \tag{A.13}$$

These equations yield closed form solutions for the three acceleration components in terms of the displacement, velocity, and forcing function components. These equations (factored slightly differently) are

$$\ddot{u}(u,v,w,\dot{u},f_u(t)) =$$
$$(1/m)\left[f_u+bk_1-\frac{b^2k_1}{b_1}-bk_2+\frac{b^2k_2}{b_2}\right.$$
$$\left.+\left(-k_1+\frac{bk_1}{b_1}-k_2+\frac{bk_2}{b_2}-k_3+\frac{bk_3}{b_3}-k_4+\frac{bk_4}{b_4}\right)u-c\dot{u}\right] \tag{A.14}$$

$$\ddot{v}(u,v,w,\dot{v},f_v(t)) =$$
$$(1/m)\left[f_v-hk_3+\frac{bhk_3}{b_3}+hk_4-\frac{bhk_4}{b_4}\right.$$
$$\left.+\left(-k_1+\frac{bk_1}{b_1}-k_2+\frac{bk_2}{b_2}-k_3+\frac{bk_3}{b_3}-k_4+\frac{bk_4}{b_4}\right)v-c\dot{v}\right] \tag{A.15}$$

$$\ddot{w}(u,v,w,\dot{w},f_w(t)) =$$
$$(1/m)\left[f_w+dk_3-\frac{bdk_3}{b_3}+dk_4-\frac{bdk_4}{b_4}+\left(-k_3+\frac{bk_3}{b_3}-k_4+\frac{bk_4}{b_4}\right)w-c\dot{w}\right] \tag{A.16}$$

These equations may be written in the form

$$[\mathbf{M}]\{\ddot{\mathbf{x}}\} + [\mathbf{C}]\{\dot{\mathbf{x}}\} + \{[\mathbf{K}]_{linear} + [\mathbf{K}]_{nonlinear}\}\{\mathbf{x}\} = \{\mathbf{f}\}_{forcing}$$

Which in expanded form is

$$\begin{bmatrix} m & 0 & 0 \\ 0 & m & 0 \\ 0 & 0 & m \end{bmatrix} \begin{Bmatrix} \ddot{u} \\ \ddot{v} \\ \ddot{w} \end{Bmatrix} + \begin{bmatrix} c & 0 & 0 \\ 0 & c & 0 \\ 0 & 0 & c \end{bmatrix} \begin{Bmatrix} \dot{u} \\ \dot{v} \\ \dot{w} \end{Bmatrix}$$

$$+ \left\{ \begin{bmatrix} p_1 & 0 & 0 \\ 0 & p_1 & 0 \\ 0 & 0 & p_2 \end{bmatrix} + \begin{bmatrix} n_1 & 0 & 0 \\ 0 & n_2 & 0 \\ 0 & 0 & n_3 \end{bmatrix} \right\} \begin{Bmatrix} u \\ v \\ w \end{Bmatrix} = \begin{Bmatrix} f_u \\ f_v \\ f_w \end{Bmatrix} \qquad \text{(A.17)}$$

where

$$\begin{aligned} p_1 &= k_1 + k_2 + k_3 + k_4 \\ p_2 &= k_3 + k_4 \\ n_1 &= b\left(-\frac{k_1}{b_1} - \frac{k_2}{b_2} - \frac{k_3}{b_3} - \frac{k_4}{b_4} - \frac{k_1}{u} + \frac{k_2}{u}\right) + b^2\left(\frac{k_1}{b_1 u} - \frac{k_2}{b_2 u}\right) \\ n_2 &= b\left(-\frac{k_1}{b_1} - \frac{k_2}{b_2} - \frac{k_3}{b_3} - \frac{k_4}{b_4} - \frac{hk_3}{b_3 v} + \frac{hk_4}{b_4 v}\right) + \frac{hk_3}{v} - \frac{hk_4}{v} \\ n_3 &= -\frac{bk_4}{b_4} + b\left(-\frac{k_3}{b_3} + \frac{dk_3}{b_3 w} + \frac{dk_4}{b_4 w}\right) - \frac{dk_3}{w} - \frac{dk_4}{w} \end{aligned} \qquad \text{(A.18)}$$

and the b_i are found in Eq (A.1).

Appendix B. *PREDCORR: Predictor-Corrector Subroutine*

This FORTRAN subroutine implements the predictor-corrector algorithm described in Section 2.2.5 on page 2-15.

```
ccccccccccccccccccccccccccccccccccccccccccccccccccccccccccccccccccccccccc
      subroutine predcorr
ccccccccccccccccccccccccccccccccccccccccccccccccccccccccccccccccccccccccc
      implicit double precision (a-h,o-z)
      common /uvw/ u0,v0,w0,udot0,vdot0,wdot0,u,v,w,udot,vdot,wdot,
     &   uddot,vddot,wddot
      common /phys/ sprngk1,sprngk2,sprngk3,sprngk4,rmass,h,b,d,c_damp
      common /forces/ f_ampl,f_freq,f_dura,fu_dir,fv_dir,fw_dir,fu,fv,
     &   fw,force_u,force_v,force_w,nftype
      common /time/ del_t,t_stop,tim,epsilon,r_load,t_ramp,del_t_last,
     &   del_t_max,del_t1,chg_t1,del_t2,chg_t2,snap_time,t_shift,ifix_t
      common /iterate/ r_iter_tot,iter,j_step,iter_max,i_snap_flag
      common /misc/ pi,rads,degs
      common /printer/ i_print,idat_print,iprn_intrvl,idat_intrvl,
     &   i_snap,j_print,jdat_print,i_screen,i_auto_try,iprn0,ipdat0,ifft
      common /old/ u_last,v_last,w_last,flast_u,flast_v,flast_w,w_tot,
     &   udot_last,vdot_last,wdot_last,uddot_last,vddot_last,wddot_last
      common /error/ err_total,pct_err_max,pct_error,top_err,
     &   top_err_tim,err_cum,rms_err,pct_err_sum,i_bif_write,i_tcheck
      common /energy/ b1,b2,b3,b4,pe_1,pe_2,pe_3,pe_4,e_potential,
     &   e_kinetic,e_pot_last,e_kin_last
      common /beta/ beta_0,beta_1,beta_2,method
      common /univ/ i_on_unv,i_unv_int,i_disp,i_vel,i_acc,icase,ncount
      common /poinc/ p_phase,tau,i_on_poin,i_poin_u,i_poin_v,i_poin_w
      common /bifur/ force_step,i_on_bifur,n_forces,n_ignore,n_capture,
     &   i_bif_step,i_forces,i_bif_u,i_bif_v,i_bif_w,i_err_flag,i_good
c
c  j_step = time step
c  iter = iteration step within time step j_step
c
      iter = 1
c       write(8,*)'iter = ',iter
c
c  for first iteration, estimate velocity at end of jth time step,
c
      udot_guess = udot + uddot*del_t
      u_guess = u + 0.5*udot*del_t + 0.5*udot_guess*del_t
c
      vdot_guess = vdot + vddot*del_t
      v_guess = v + 0.5*vdot*del_t + 0.5*vdot_guess*del_t
c
      wdot_guess = wdot + wddot*del_t
      w_guess = w + 0.5*wdot*del_t + 0.5*wdot_guess*del_t
c
      call a_calc(u_guess,v_guess,w_guess,udot_guess,vdot_guess,
     &               wdot_guess,uddot_guess,vddot_guess,wddot_guess)
c
c  for iterations greater than first...
c
   20 udot_guess = udot + 0.5*uddot*del_t + 0.5*uddot_guess*del_t
```

```
      ulast = u_guess
      u_guess = u + 0.5*udot*del_t + 0.5*udot_guess*del_t
c
      vdot_guess = vdot + 0.5*vddot*del_t + 0.5*vddot_guess*del_t
      vlast = v_guess
      v_guess = v + 0.5*vdot*del_t + 0.5*vdot_guess*del_t
c
      wdot_guess = wdot + 0.5*wddot*del_t + 0.5*wddot_guess*del_t
      wlast = w_guess
      w_guess = w + 0.5*wdot*del_t + 0.5*wdot_guess*del_t
c
      call a_calc(u_guess,v_guess,w_guess,udot_guess,vdot_guess,
     &               wdot_guess,uddot_guess,vddot_guess,wddot_guess)
c
c  check for convergence
c
   30 epschk2 = dsqrt( u_guess**2 + v_guess**2 + w_guess**2)
      epschk1 = dsqrt( ulast**2 + vlast**2 + wlast**2)
      epschk3 = dabs(epschk2 - epschk1)
      epschk4 = epsilon*epschk2
      if (epschk3 .gt. epschk4) then
         if (i_print .eq. 1 .and. j_print .eq. iprn_intrvl)
     &        write(8,*)'iter = ',iter,'    epschk3 = ',epschk3
         if (iter .gt. iter_max) then
            if (i_auto_try .ne. 1) then
               call report_it
               stop
            end if
            i_err_flag = 2
            call err_hndlr
            return
         end if
c         write(20,1000)j_step,iter,w_guess
         iter = iter + 1
         r_iter_tot = r_iter_tot + 1.0
         goto 20
      end if
   40 if (i_print .eq. 1 .and. j_print .eq. iprn_intrvl)
     &   write(8,*)'iter = ',iter,'    epschk3 = ',epschk3
      u_last = u
      v_last = v
      w_last = w
      u = u_guess
      v = v_guess
      w = w_guess
      udot = udot_guess
      vdot = vdot_guess
      wdot = wdot_guess
      uddot = uddot_guess
      vddot = vddot_guess
      wddot = wddot_guess
 1000 format(1x,i5,1x,i4,1x,e12.5)
      return
      end
```

Appendix C. *CHECK_IT: Energy Checking Subroutine*

This FORTRAN subroutine implements the energy checking scheme described in Section 2.2.4 on page 2-13.

```
ccccccccccccccccccccccccccccccccccccccccccccccccccccccccccccccccccccccccc
      subroutine check_it
ccccccccccccccccccccccccccccccccccccccccccccccccccccccccccccccccccccccccc
      implicit double precision (a-h,o-z)
      common /uvw/ u0,v0,w0,udot0,vdot0,wdot0,u,v,w,udot,vdot,wdot,
     &   uddot,vddot,wddot
      common /phys/ sprngk1,sprngk2,sprngk3,sprngk4,rmass,h,b,d,c_damp
      common /forces/ f_ampl,f_freq,f_dura,fu_dir,fv_dir,fw_dir,fu,fv,
     &   fw,force_u,force_v,force_w,nftype
      common /time/ del_t,t_stop,tim,epsilon,r_load,t_ramp,del_t_last,
     &   del_t_max,del_t1,chg_t1,del_t2,chg_t2,snap_time,t_shift,ifix_t
      common /iterate/ r_iter_tot,iter,j_step,iter_max,i_snap_flag
      common /misc/ pi,rads,degs
      common /printer/ i_print,idat_print,iprn_intrvl,idat_intrvl,
     &   i_snap,j_print,jdat_print,i_screen,i_auto_try,iprn0,ipdat0,ifft
      common /old/ u_last,v_last,w_last,flast_u,flast_v,flast_w,w_tot,
     &   udot_last,vdot_last,wdot_last,uddot_last,vddot_last,wddot_last
      common /error/ err_total,pct_err_max,pct_error,top_err,
     &   top_err_tim,err_cum,rms_err,pct_err_sum,i_bif_write,i_tcheck
      common /energy/ b1,b2,b3,b4,pe_1,pe_2,pe_3,pe_4,e_potential,
     &   e_kinetic,e_pot_last,e_kin_last
      common /beta/ beta_0,beta_1,beta_2,method
      common /univ/ i_on_unv,i_unv_int,i_disp,i_vel,i_acc,icase,ncount
      common /poinc/ p_phase,tau,i_on_poin,i_poin_u,i_poin_v,i_poin_w
      common /bifur/ force_step,i_on_bifur,n_forces,n_ignore,n_capture,
     &   i_bif_step,i_forces,i_bif_u,i_bif_v,i_bif_w,i_err_flag,i_good
c
c  calculate potential energy of system by spring
c
      call b_calc(u,v,w)
c
      pe_1 = 0.5*sprngk1*( b1 - b )**2
      pe_2 = 0.5*sprngk2*( b2 - b )**2
      pe_3 = 0.5*sprngk3*( b3 - b )**2
      pe_4 = 0.5*sprngk4*( b4 - b )**2
c
      e_potential = pe_1 + pe_2 + pe_3 + pe_4
c
c  calculate kinetic energy of rmass
c
      e_kinetic = 0.5*rmass * ( udot**2 + vdot**2 + wdot**2 )
c
c  calculate change in energies over time step
c
      del_e_pot = e_potential - e_pot_last
      del_e_kin = e_kinetic - e_kin_last
      delta_e = del_e_pot + del_e_kin
c
c  calculate increment of work done by applied load
c
```

```
c   calculate displacement over last increment
c
      del_u = u - u_last
      del_v = v - v_last
      del_w = w - w_last
c      write(10,*)'del_?--> u=',del_u,' v=',del_v,' w=',del_w
c
c   calculate work done over last increment using avg force over step
c
      work_u = 0.5*(force_u + flast_u) * del_u
      work_v = 0.5*(force_v + flast_v) * del_v
      work_w = 0.5*(force_w + flast_w) * del_w
      del_work = work_u + work_v + work_w
c      write(10,*)'work_?--> u=',work_u,' v=',work_v,' w=',work_w
c
c   add to total work done
c
      w_tot = w_tot + del_work
c
c  take sum (should remain constant thoughout run in undamped case)
c
      err_step = dabs(del_work - del_e_pot - del_e_kin)
      err_cum = err_cum + err_step
c
c  calculate percent error
c
      if(w_tot .gt. 1.0D-10)pct_error = dabs(err_cum/w_tot)*100.
      pct_err_sum = pct_err_sum + pct_error**2
      rms_err = dsqrt(pct_err_sum/j_step)
      if (rms_err .gt. top_err) then
         top_err = rms_err
         top_err_tim = tim
      end if
c
c  check for exceeding pct_err_max
c
      if (rms_err .gt. pct_err_max) then
         i_err_flag = 1
         if (i_auto_try .ne. 1)then
           call report_it
           stop
         end if
         call err_hndlr
         return
      end if
c
c      write(10,*)'w_tot= ',' e_kinetic= ',e_kinetic
c      write(10,*)'e_potential= ',e_potential,' err_total= ',err_total
      return
      end
```

Bibliography

1. Almroth, B.L. et al., *User Instructions for STAGSC-1, Volume II.* LMSC-DG33873, January 1983.
2. Baker, Gregory L. and Gollub, Jerry P. *Chaotic Dynamics: an Introduction.* Cambridge: Cambridge University Press, 1990.
3. Blachman, Nancy R., Mathematica*: A Practical Approach.* Englewood Cliffs, N.J.: Prentice-Hall, 1992.
4. Blair, Kim B., et al. "Nonlinear Dynamic Response of Shallow Arches," AIAA-92-2548-CP, 2376–2384, 1992.
5. Boyce, William E. and DePrima, Richard C. *Elementary Differential Equations and Boundary Value Problems* (3rd edition). New York: John Wiley & Sons, 1977.
6. Chien, L.S., and Palazotto, A.N., "Dynamic Buckling of Composite Cylindrical Panels with High-Order Transverse Shears Subjected to a Transverse Concentrated Load," *International Journal of Non-Linear Mechanics, 27, No. 5*:719–734, (1992).
7. Chien, L.S., and Palazotto, A.N., "Nonlinear Snapping Considerations for Laminated Cylindrical Panels," *Composites Engineering, 2, No. 8*:631–639, (1992).
8. Cook, Robert D. et al., *Concepts and Applications of Finite Element Analysis.* New York: John Wiley & Sons, 1989.
9. Dennis, Scott, T., *Large Displacement and Rotational Formulation for Laminated Cylindrical Shells Including Parabolic Transverse Shear.* Ph.D. Dissertation, AFIT/DS/AA/88-1. School of Engineering, Air Force Institute of Technology (AU), Wright Patterson Air Force Base, OH. 1988.
10. El Naschie, M.S., *Stress, Stability and Chaos in Structural Engineering: An Energy Approach.* Berkshire, England: McGraw-Hill, 1990.
11. Higgins, R.J., "Fast Fourier transform: An Introduction with some minicomputer experiments," *American Journal of Physics, 44, No. 8*:766–773, (Aug 1976).
12. Hornbeck, Robert W., *Numerical Methods.* New York: Quantum Publishers, Inc., 1975.
13. Katona, M.G., and Zienkiewicz, O.C., "A Unified Set of Single Step Algorithms, Part 3: The Beta-*m* Method, A Generalization of the Newmark Scheme," *International Journal for Numerical Methods In Engineering, 21, No. 7*:1345–1359, (1985).
14. Kounadis, A.N., "Chaoslike Phenomena in the Non-Linear Dynamic Stability of Discrete Damped or Undamped Systems Under Step Loading," *International Journal of Nonlinear Mechanics, 26, No. 3/4*:103–311, (1991).
15. Low, K.H., "On the Accuracy of the Numerical Integral for the Analysis of Dynamic Response," *Computers & Structures, 44, No. 3*:549–556, (1991).
16. Maestrello, Lucio, et al., "Nonlinear Vibration and Radiation from a Panel with Transition to Chaos", *AIAA Journal, 30, No. 11*:2632–2638, (1992).
17. Moon, Francis C., *Chaotic Vibrations: An Introduction for Applied Scientists and Engineers.* New York: John Wiley & Sons, 1987.
18. Palazotto, A.N. et al., "Stability Characteristics of Laminated Cylindrical Panels Under Transverse Loading", *AIAA Journal, 30, No. 6*:1649–1653, (1992).

19. Palazotto, A.N., and Dennis, Scott T., *Nonlinear Analysis of Shell Structures.* Washington, D.C.: American Institute of Aeronautics and Astronautics, Inc., 1992.

20. Raouf, R.A., and Palazotto, A.N., "Non-linear free vibrations of symmetrically laminated, slightly compressible cylindrical shell panels," *Composite Structures, 20*:249–257, (1992).

21. Raouf, R.A., and Palazotto, A.N., "Nonlinear Dynamic Response of Anisotropic, Arbitrarily Laminated Shell Panels: An Asymptotic Analysis," *Composite Structures, 18*:163–192, (1991).

22. Reddy, J.N., and Liu, C.F., "A Higher Order Shear Deformation Theory of Laminated Composite Shells," *International Journal of Engineering Science, 23, No. 3*:319–330, (1985).

23. Riks, E., "An incremental approach to the solution of snapping and buckling problems," *Int. J. Solids Structures, 15*:529–551, (1979).

24. Saada, Adele S., *Elasticity Theory and Applications.* New York: Pergamon Press, 1989.

25. Silva, K.J., *Finite Element Investigation of a Composite Cylindrical Shell Under Transverse Load with Through Thickness Shear and Snapping.* M.S. Thesis, AFIT/GAE/ENY/89D-35. School of Engineering, Air Force Institute of Technology (AU), Wright Patterson AFB, OH, 1989.

26. Simitses, George J., *Dynamic Stability of Suddenly Loaded Structures,* New York: Springer-Verlag, 1990.

27. Smith, Randy A. *Higher-Order Thickness Expansions for Cylindrical Shells.* Ph.D. Dissertation, AFIT/DS/ENY/91-1. School of Engineering, Air Force Institute of Technology (AU), Wright-Patterson AFB, OH, September 1991.

28. Taylor Jr., Walter W., *Finite Element Investigation into the Dynamic Instability Characteristics of Laminated Composite Panels,* M.S. Thesis, AFIT/GAE/ENY/90D-28. School of Engineering, Air Force Institute of Technology (AU), Wright Patterson AFB, OH, 1990.

29. Thompson, J.M.T., *Nonlinear Dynamics and Chaos.* Chichester, England, U.K.: John Wiley & Sons, 1986.

30. Tsai, C.T., and Palazotto, A.N. "On the Finite Element Analysis of Non-Linear Vibration for Cylindrical Shells with High-Order Shear Deformation Theory," *International Journal of Non-Linear Mechanics, 26, No. 3/4*:379–388, (1991).

31. Weaver Jr., William et al. *Vibration Problems in Engineering* (Fifth Edition). New York: John Wiley & Sons, 1990.

32. Zeng, X., et al., "Estimating the Lyapunov-Exponent Spectrum from Short Time Series of Low Precision", *Physical Review Letters, 66, No. 25*:3229–3232, (1991).

Vita

Captain James M. Greer Jr was born on 16 February 1959 at Westover Air Force Base, Chicopee Falls, Massachusetts. He graduated from high school in Camp Springs, Maryland in 1977 and attended Western Kentucky University, Embry-Riddle Aeronautical University, and the University of Florida. Captain Greer earned his Bachelor of Science Degree in Engineering (Aerospace Engineering) from the University of Florida in 1983, and was commissioned through Officer Training School. He was then stationed at what is now the Wright Laboratory's Aeropropulsion Laboratory. In 1987, Captain Greer was transferred to Electronic Systems Division, Hanscom Air Force Base, Massachusetts working in various strategic program offices. He entered the Air Force Institute of Technology, School of Engineering, in May, 1991.

Permanent address: *1521-C Sudbury Ln*
Fairborn, Ohio 45324-6529

REPORT DOCUMENTATION PAGE

Form Approved
OMB No 0704-0188

1. AGENCY USE ONLY (Leave blank)	2. REPORT DATE	3. REPORT TYPE AND DATES COVERED
	15 December 1992	Master's Thesis

4. TITLE AND SUBTITLE

THE NON-LINEAR DYNAMICS OF COMPOSITE CYLINDRICAL SHELLS

5. FUNDING NUMBERS

6. AUTHOR(S)

James M. Greer, Jr.
Captain, USAF

7. PERFORMING ORGANIZATION NAME(S) AND ADDRESS(ES)

Air Force Institute of Technology
WPAFB OH 45433-6583

8. PERFORMING ORGANIZATION REPORT NUMBER

AFIT/GAE/ENY/92D-06

9. SPONSORING / MONITORING AGENCY NAME(S) AND ADDRESS(ES)

Mr Nelson Wolf
Wright Laboratories (WL/FIBR)
WPAFB OH 45433-5000

10. SPONSORING / MONITORING AGENCY REPORT NUMBER

11. SUPPLEMENTARY NOTES

12a. DISTRIBUTION / AVAILABILITY STATEMENT

Approved for public release; distribution unlimited

12b. DISTRIBUTION CODE

13. ABSTRACT *(Maximum 200 words)*

The non-linear dynamic behavior of suddenly loaded composite shells is the subject of this research. The objective of the research is two-fold: (1) to characterize the apparently random physical behavior sometimes observed in the finite element analysis as either numerical instability, chaotic behavior, or both; and (2) to develop criteria for choosing time steps for the finite element model, referred to as DSHELL. This displacement based finite element code is capable of dynamic analysis of plates, arches, and cylindrical shells undergoing large displacements and moderately large rotations during deformation. DSHELL uses a 36-DOF isoparametric shell element to obtain numerical results. A simplified shell model (MSHELL) is developed to provide a shell analog that requires much less computer time to run than the full-up finite element model. The results of the investigations using this simplified model are then applied toward understanding behavior seen in the finite element code. The simplified model and the composite shell exhibit chaotic behavior after collapse. For loads not sufficient to cause collapse, the composite shell experiences oscillations at the panel edges of a type associated with near-chaotic behavior. Significant in-plane oscillations (parametric resonances) are exhibited by the suddenly-loaded composite shell. Extensive use of the *Fast Fourier Transform* (FFT) is made to investigate behavior of the MSHELL and DSHELL models in the frequency domain. The composite shell is compared to an isotropic shell of identical physical dimensions and static collapse strength, showing the primary effect of isotropy to be increased flexibility in all displacement directions. A method is developed using MSHELL for choosing appropriate time steps for analyses using DSHELL.

14. SUBJECT TERMS

Nonlinear Analysis, Nonlinear Dynamics, Chaos, Finite Element Analysis, Shells, Structural Mechanics, Composites, Numerical Methods

15. NUMBER OF PAGES

107

16. PRICE CODE

17. SECURITY CLASSIFICATION OF REPORT	18. SECURITY CLASSIFICATION OF THIS PAGE	19. SECURITY CLASSIFICATION OF ABSTRACT	20. LIMITATION OF ABSTRACT
Unclassified	Unclassified	Unclassified	UL